

Non-linear conjugate gradient inversion for global EM induction: resolution studies

Anna Kelbert,¹ Gary D. Egbert¹ and Adam Schultz^{1,2}

¹College of Oceanic and Atmospheric Sciences, Oregon State University, 104 COAS Admin Bldg, Corvallis, OR 97331-5503, USA

E-mail: anya@coas.oregonstate.edu

²Division of Ocean Science, Room 725, National Science Foundation, 4201 Wilson Blvd., Arlington, VA 22230, USA

Accepted 2007 December 20. Received 2007 September 20; in original form 2007 May 16

SUMMARY

We develop a non-linear conjugate gradient inversion for global long period electromagnetic induction studies. The scheme requires computation of derivatives of the regularized penalty functional. We derive analytical and numerical expressions for these derivatives, and the associated Jacobian, and show how these can be efficiently implemented by generalizing and extending an existing finite difference forward solver. Using layered spherical harmonics to parametrize the model space, we invert a range of synthetic data sets to test the inversion, and to study vertical and horizontal resolution of currently available data sets. We conclude that the currently available long-period global geomagnetic observatory data in the period range 5–107 d can resolve large scale (300–500 km vertically, thousands of km horizontally) heterogeneities in mantle electrical conductivity reliably at depths \sim 670–1600 km. By extending induction response to 0.2–5 d (including daily variation periods), upper-mantle structure could also be resolved.

Key words: Numerical solutions; Inverse theory; Electrical properties; Non-linear electromagnetics; Geomagnetic induction; Composition of the mantle.

1 INTRODUCTION

Seismic tomographic studies (Jordan 1975; Su & Dziewonski 1992; Woodward *et al.* 1993; Romanowicz 2003, and many others) have shown large lateral changes in seismic velocities throughout the mantle. There are several possible causes for such heterogeneities, including variations in chemical composition and temperature associated with convection (Boehler 1996), and the introduction of water and volatiles into the mantle by descending slabs (Lay 1994). Each of these factors is a strong reason also to expect 3-D heterogeneities in mantle electrical conductivity. Additionally, laboratory results applied to samples of wet and dry olivine and other upper-mantle minerals (e.g. Hirsch & Shankland 1993b; Hirsch *et al.* 1993; Xu *et al.* 1998; Sakamaki *et al.* 2006) argue in favour of even stronger lateral heterogeneities in upper-mantle electrical conductivity.

Indeed, it has long been established formally that no global 1-D model exists that fits all global magnetic observatory data sets to within statistical bounds (Schultz & Larsen 1990), and that the observed geographic variability of long-period ($T > 5$ d) geomagnetic data cannot be explained by the contrast in electrical conductivity between oceans and continents (Kuvshinov *et al.* 1990; Tarits 1994; Everett *et al.* 2003). Strong lateral variations are also implied by differences between sets of deep, regional 1-D magnetotelluric soundings that were made possible by very long-period observations using long electric dipoles (Egbert & Booker 1992; Bahr *et al.* 1993; Schultz *et al.* 1993) and abandoned submarine telecommunications cables (Lizarralde *et al.* 1995; Koyama *et al.* 2003; Utada *et al.* 2003;

Kuvshinov *et al.* 2005). However, it is only recently that the rapid growth of computational resources has made 3-D electromagnetic (EM) inversion practical. Here we describe development and initial application of a 3-D EM inversion algorithm based on non-linear conjugate gradients.

Frequency domain forward solutions in spherical geometry developed and implemented in the last two decades include a semi-analytic method based on the perturbation expansion of conductivity about a background 1-D model (Zhang 1991), finite elements (Everett & Schultz 1996; Weiss & Everett 1998; Yoshimura & Oshiman 2002), spherical harmonics combined with finite elements (Martinec 1999), spectral (Grammatica & Tarits 2002), heterogeneous integral equations (Kuvshinov & Pankratov 1994; Koyama *et al.* 2003; Kuvshinov *et al.* 2005) and staggered-grid finite difference (Uyeshima & Schultz 2000). Time domain techniques, based on spherical harmonic expansions (Hamano 2002; Velimsky *et al.* 2003; Velimsky & Martinec 2005) have also been developed for computing 3-D EM fields of a transient external source.

For our inversion we use the 3-D frequency domain forward solver of Uyeshima & Schultz (2000) and Toh *et al.* (2002). This solver employs a staggered-grid finite difference formulation in spherical coordinates, analogous to the Cartesian formulation of Mackie & Madden (1993a,b). The induced magnetic fields are found as a solution to the integral form of Maxwell's equations, with the system of linear equations resulting from discretization solved using stabilized biconjugate gradients. The solver has been carefully tested and cross-compared against the numerical solution of Kuvshinov

& Pankratov (1994) and the quasi-analytic solution of Martinez (1998), and assessed to be accurate and efficient enough to be an attractive kernel of a practical inversion scheme. Here we develop such a scheme for inversion of frequency-domain magnetic (or magnetotelluric) transfer functions.

A number of regional (e.g. Egbert & Booker 1992; Schultz *et al.* 1993; Olsen 1999; Neal *et al.* 2000; Ichiki *et al.* 2001; Utada *et al.* 2003) and global (Constable & Constable 2004; Kuvshinov & Olsen 2006; Velimsky *et al.* 2006) 1-D inversions of observatory and satellite data have been previously presented. The only inverse solution for global 3-D conductivity we are aware of (Schultz & Pritchard 1999) was based on inversion of the augmented Schultz & Larsen (1987) global Z/H data set. The forward modelling approach used for this inversion was accurate only for small perturbations about a prior 1-D model, and it was found that no model satisfying this limitation could fit the European subset of observatories. A regional mantle scale joint inversion of submarine cable data and near-shore observatory data has been performed recently for the area beneath the North Pacific (Koyama *et al.* 2003), and 3-D perturbations around the prior 1-D model of Utada *et al.* (2003) have been obtained in this region.

A number of newly available data sources, which may potentially provide better constraints on 3-D mantle electrical conductivity variations, have not to date been inverted for mantle structure. For example, Fujii & Schultz (2002) have compiled an improved and expanded set of observatory response functions. In addition, a number of new observatories have been installed in recent years, potentially providing better coverage, particularly in the southern hemisphere. In future, satellite data (Olsen *et al.* 2006) may provide significantly better spatial coverage, particularly in the ocean basins (Kuvshinov *et al.* 2006).

Here, we present a fully 3-D inverse tool for global geoelectromagnetic sounding. We develop a numerical scheme that allows us to evaluate data sensitivities efficiently, and to implement a regularized non-linear conjugate gradients (NLCG) inversion. To speed up gradient evaluations we use an adjoint approach, similar to that discussed in Rodi & Mackie (2001) and Newman & Boggs (2004). For the inversion, the Earth's mantle is parametrized in terms of a series of heterogeneous layers, each expanded in spherical harmonics. We discuss the spatial resolution of our method for a number of synthetic examples, and show that an NLCG inversion of data sets with sufficiently broad frequency content could indeed resolve the large-scale 3-D distribution of electrical conductivity in the mantle, which is currently only marginally known. In a future work, we will report on the application of the method described here to the Fujii & Schultz (2002) data set.

2 INVERSE APPROACH

2.1 Formulation

We solve the regularized least-squares inverse problem, with the penalty functional defined by

$$R(\mathbf{m}) = (\psi(\mathbf{m}) - \mathbf{d})^H \mathbf{C}_d^{-1} (\psi(\mathbf{m}) - \mathbf{d}) + \lambda(\mathbf{m} - \mathbf{m}_0)^T \mathbf{C}_m^{-1} (\mathbf{m} - \mathbf{m}_0). \quad (1)$$

Here $\mathbf{m}, \mathbf{m}_0 \in \mathbb{R}^M$ are vectors representing, respectively, the model parameters and the prior; $\mathbf{d} \in \mathbb{C}^N$ is the data vector; $\psi: \mathbb{R}^M \rightarrow \mathbb{C}^N$ are non-linear data functionals; and λ is a damping parameter. Note that the data space is in general complex, while the model space is real. Additionally, $\mathbf{C}_d: \mathbb{C}^N \rightarrow \mathbb{C}^N$ and $\mathbf{C}_m: \mathbb{R}^M \rightarrow \mathbb{R}^M$ are

data and model covariance operators; and the subscript H denotes the Hermitian conjugate transpose. In our analysis, we take \mathbf{C}_d to be diagonal, such that \mathbf{C}_d^{-1} scales by the inverse of the data error variance.

We can say that a model ‘fits the data’ if the squared normalized data misfit norm

$$R_d(\mathbf{m}) = [\psi(\mathbf{m}) - \mathbf{d}]^H \mathbf{C}_d^{-1} [\psi(\mathbf{m}) - \mathbf{d}] \quad (2)$$

is sufficiently close to its expected value, that is, the number of independent data components. We obtain the inverse solution by minimizing the model norm

$$R_m = (\mathbf{m} - \mathbf{m}_0)^T \mathbf{C}_m^{-1} (\mathbf{m} - \mathbf{m}_0) \quad (3)$$

subject to fitting the data as defined by (2), within a specified tolerance. For a fixed value of λ , a stationary point of (1) corresponds to a local minimum of the model norm R_m , subject to the achieved data misfit R_d (e.g. Parker 1994).

2.2 Forward problem

The forward solver (Uyeshima and Schultz 2000; henceforth U&S) is effectively equivalent to a numerical solution of the vector Helmholtz equation for the magnetic field \mathbf{H} , assuming harmonic time dependence of the form $e^{i\omega t}$,

$$\nabla \times (\rho \nabla \times \mathbf{H}) + i\omega\mu_0 \mathbf{H} = 0 \quad (4)$$

in a computational domain that includes the resistive air and conductive Earth's oceans, crust and mantle. Here, \mathbf{H} denotes the magnetic field, ρ is the electrical resistivity, ω is frequency, and μ_0 is the vacuum magnetic permeability. Note that the electrical resistivity of the air is set to a moderately large finite value of $10^{10} \Omega\text{m}$ (see Mackie & Madden 1993b), so that the Helmholtz equation holds throughout the model domain, while the resulting numerical system remains acceptably well conditioned. To complete the system, the tangential components of the magnetic field \mathbf{H} at the upper and lower boundaries of the domain are specified.

A staggered-grid finite difference method is used to solve (4) numerically. In the U&S formulation, the computational domain is subdivided into curved rectangular prisms, such that the components of \mathbf{H} are defined on the edges. The linear system of equations involving the components of \mathbf{H} is symmetric and real everywhere except along the diagonal. A variant of biconjugate gradients (BiCGStab, Toh *et al.* 2002) is used to obtain the solution iteratively. As in Mackie *et al.* (1994) and Smith (1996), a divergence correction is applied as part of the iterative scheme to avoid accumulation of error in the value of $\nabla \cdot \mathbf{H}$, which should be identically zero.

The lower boundary is set at or just below the core-mantle boundary (CMB; $\sim 2890 \text{ km}$), where we set the tangential components of \mathbf{H} to zero. As in U&S, here we assume that the equatorial ring current is the primary source of the geomagnetic variations, approximating the inducing sources of D_{st} -type by a P_1^0 spherical harmonic (e.g. Banks & Ainsworth 1992). The source is specified at the upper boundary of the computational domain, placed at a radial distance from the Earth's surface of $r = 10 R_e$, where R_e is the Earth's radius. At this distance, secondary magnetic fields induced by the presence of the conductive Earth are damped out to $< 10^{-3}$ of the external field intensity and may be considered negligible (U&S, Appendix).

2.3 Global geomagnetic responses

According to the geomagnetic depth sounding (GDS) on a point method the scalar c response (Banks 1969; Schmucker 1970; Schultz

& Larsen 1987) at a single observatory and a single angular frequency ω may be defined as

$$c(\omega) = \frac{a \tan(\theta)}{2} \frac{H_r(\omega)}{H_\theta(\omega)}, \quad (5)$$

where a is the radius of the Earth in metres, ω is the angular frequency, θ is geomagnetic colatitude in radians, H_r is the vertical component of the magnetic field pointing downwards to the centre of the Earth, and H_θ is the colatitudinal component pointing to magnetic south. This definition of c response was originally devised for a radially symmetric Earth under the assumption of a P_1^0 -form external source. The term $\tan(\theta)$ in (5) compensates for the spatial structure of the source, so the c response would be the same everywhere on the surface of a 1-D spherical Earth. The c response has units of length and a positive real part, and provides a convenient means to estimate depth of penetration of the externally induced fields into the Earth's interior. However, once the spherical symmetry assumption is violated, H_r will not in general be zero at the equator, and the singularity of $\tan(\theta)$ at $\theta = 90^\circ$ makes the c response undefined at this colatitude. We avoid the singularity by leaving out the source field colatitude compensation and work with c ratios,

$$c_r(\omega) = \frac{a}{2} \frac{H_r(\omega)}{H_\theta(\omega)}, \quad (6)$$

rather than the standard c responses. In fact, for actual data the source compensation term $\tan(\theta)$ multiplies both the data and the standard deviation, and thus exactly cancels out in the penalty functional (1). In the same way we modify the d responses of Fujii & Schultz (2002) to d ratios

$$d_r(\omega) = \frac{a}{2} \frac{H_\phi(\omega)}{H_\theta(\omega)}, \quad (7)$$

where H_ϕ is the longitudinal component of the magnetic field pointing to magnetic east. This component is zero if the mantle is 1-D and the source is zonal. Therefore, non-zero values of d ratios arise under such excitation only in the presence of lateral conductivity heterogeneities. Here we consider explicitly inversion of c and d ratios. Extension to treat other possible sorts of long period EM data would be straightforward.

2.4 Model parametrization

The region from 12.65 km depth to the CMB is subdivided vertically into layers (generally, 8–20), with electrical resistivity in each layer parametrized using spherical harmonics,

$$\log_{10} \rho_k(\theta, \phi) = a_0^0 + \sum_{l=1}^L \left[a_l^0 P_l(\cos \theta) + \left[\sum_{m=1}^l a_l^m \cos(m\phi) + \sum_{m=-1}^{-l} a_l^m \sin(m\phi) \right] S_l^m(\cos \theta) \right], \quad (8)$$

where S_l^m are Schmidt semi-normalized associated Legendre functions (Schmidt 1895), and k is the layer index. The corresponding section of the model parameter vector can be written as

$$\mathbf{m}^{(k)} = \{a_0^0, a_1^0, a_1^1, a_2^0, a_2^1, a_2^{-1}, a_2^2, a_2^{-2}, \dots\}. \quad (9)$$

The resistivity of the uppermost 12.65 km is kept fixed, unless otherwise specified, it is based on a near-surface conductance map (S-map), provided by A. Kuvshinov (personal communication, 2004), resampled on to the numerical grid.

In practice, the model covariance is designed to penalize large deviations from the starting model parameters, and other features such

as large jumps between neighbouring layers and higher order terms that correspond to finer detail in the model. The standard approach (e.g. Rodi & Mackie 2001; Haber *et al.* 2004) is to regularize directly in terms of \mathbf{C}_m^{-1} , that is often easy to implement. In this case, however, the model norm (3) has an unbounded eigenvalue spectrum, making the overall penalty functional very poorly conditioned, and potentially difficult to minimize without pre-conditioning. On the other hand, the model covariance operator $\mathbf{C}_m : \mathbb{R}^M \rightarrow \mathbb{R}^M$ could be considered a smoothing operator.

Since \mathbf{C}_m is symmetric and positive-semidefinite, there is a symmetric invertible linear operator $\mathbf{C}_m^{1/2}$ such that $\mathbf{C}_m = \mathbf{C}_m^{1/2} \mathbf{C}_m^{1/2}$. Setting

$$\hat{\mathbf{m}} = \mathbf{C}_m^{-1/2}(\mathbf{m} - \mathbf{m}_0), \quad (10)$$

the expression (1) for the least-squares penalty functional may be rewritten in terms of $\hat{\mathbf{m}}$:

$$R(\hat{\mathbf{m}}) = [\psi(\mathbf{C}_m^{1/2} \hat{\mathbf{m}} + \mathbf{m}_0) - \mathbf{d}]^H \mathbf{C}_d^{-1} [\psi(\mathbf{C}_m^{1/2} \hat{\mathbf{m}} + \mathbf{m}_0) - \mathbf{d}] + \lambda \hat{\mathbf{m}}^T \hat{\mathbf{m}}. \quad (11)$$

After minimizing (11) over $\hat{\mathbf{m}}$, the transformation $\mathbf{m} = \mathbf{C}_m^{1/2} \hat{\mathbf{m}} + \mathbf{m}_0$ takes us back into the space of the original model parametrization. The minimizers of (11) and (1) are identical, but formulated as in (11) the inverse problem is regularized in the sense of Tikhonov (1963). Thus, by solving the problem in the space of $\hat{\mathbf{m}}$, we achieve pre-conditioning comparable to that used by Rodi & Mackie (2001) or Haber *et al.* (2000) at no additional computational cost. Note that this scheme only requires the smoothing operator $\mathbf{C}_m^{1/2}$. The corresponding inverse, which may be very difficult to implement, is never required.

The model covariance is implemented as a combination of horizontal and vertical smoothing operators, \mathbf{C}_H and \mathbf{C}_V , such that the symmetric ‘square root’ model covariance is,

$$\mathbf{C}_m^{1/2} = \mathbf{C}_V \mathbf{C}_H \mathbf{C}_V. \quad (12)$$

Here, \mathbf{C}_H implements multiplication by $c_l = l^{-\alpha/2}$, $\alpha > 0$, and downweights the effect of higher order spherical harmonic terms. Regularization across layer boundaries is implemented by operator \mathbf{C}_V , which acts on a vector of parameters for a fixed (l, m) harmonic across the layers. In our implementation,

$$\mathbf{C}_V = \begin{pmatrix} \beta_1 & \frac{1-\beta_1}{2} & & & \\ \frac{1-\beta_1}{2} & \beta_2 & \frac{1-\beta_2}{2} & & 0 \\ & \frac{1-\beta_2}{2} & \beta_3 & & \\ & & & \ddots & \\ 0 & & \frac{1-\beta_{n-2}}{2} & \beta_{n-1} & \frac{1-\beta_{n-1}}{2} \\ & & & \frac{1-\beta_{n-1}}{2} & \beta_n \end{pmatrix}, \quad (13)$$

with $0 \leq \beta_i \leq 1$, $i = 1, \dots, n$. Smoothing between layers i and $i+1$ may be turned off by setting $\beta_i = 1$.

2.5 Non-linear conjugate gradient technique

We seek the inverse solution by an iterative process of minimizing (1) for a fixed value of λ , then reducing λ (by a factor of 10) when the misfit R_d stops decreasing. The process is terminated when the target data misfit is achieved (generally, 1 for the normalized misfit) or when reduction of data misfit stalls.

For a fixed damping parameter λ , the minimization of the penalty functional (11) is achieved by the non-linear Polak-Ribière conjugate gradients technique with line search based on a secant method.

The Hessian of the penalty functional is approximated by first derivatives and substituted in the Taylor's expansion to estimate the line search step size parameter. The line search direction is recomputed and the line search performed repeatedly until the norm of the gradient is lower than some threshold. Our implementation follows mostly Press *et al.* (1992) and Shewchuk (1994).

The NLCG approach requires evaluation of both the penalty functional and the gradient of the penalty functional with respect to the model parameters at each step of the iterative process. From (11), it follows that

$$\left[\frac{\partial R}{\partial \hat{\mathbf{m}}} \right]^T = 2 \operatorname{Re} \left(\left[\frac{\partial \psi}{\partial \hat{\mathbf{m}}} \right]^H \mathbf{C}_d^{-1} [\psi(\mathbf{C}_m^{1/2} \hat{\mathbf{m}} + \mathbf{m}_0) - \mathbf{d}] \right) + 2\lambda \hat{\mathbf{m}}. \quad (14)$$

Here, $\partial \psi / \partial \hat{\mathbf{m}}$ is the Jacobian of the forward modelling operator, that is, a complex $N \times M$ matrix of data sensitivities, where N is the number of data, and M is the dimension of the model parameter space. It can be seen from eq. (14), that the NLCG approach requires a calculation of the product of the (adjoint) Jacobian with the normalized residual. Computation of this product does not require the full Jacobian matrix. Representation of the Jacobian as a combination of linear operators allows for an efficient implementation of this calculation, as we now describe.

3 SENSITIVITY CALCULATIONS

3.1 Formulation of data sensitivities

The model response $\psi_j(\mathbf{m})$ for a single observation d_j can be written

$$\psi_j = \psi_j(\mathbf{m}) = \varphi_j\{\gamma_{\omega,s}[\eta(\mathbf{m})]\}, \quad (15)$$

where $\eta(\mathbf{m}) = \rho$ is the electrical resistivity on the grid; $\gamma_{\omega,s}(\rho) = \mathbf{h}$ is the forward solver, that maps the grid resistivity to the magnetic field components on the grid, for frequency ω and source field s ; and $\varphi_j(\mathbf{h}) = \psi_j$ denote the data functionals.

Using the chain rule:

$$\frac{\partial \psi_j}{\partial \mathbf{m}} = \frac{\partial \psi_j}{\partial \mathbf{h}} \frac{\partial \mathbf{h}}{\partial \rho} \frac{\partial \rho}{\partial \mathbf{m}}, \quad (16)$$

where $\partial \psi_j / \partial \mathbf{m}$ is a row vector that relates a variation in the data functional to small perturbations in each of the model parameters m_i , $i = 1, \dots, M$. The full Jacobian $\partial \psi / \partial \mathbf{m}$, computed for a single frequency ω , is an $N \times M$ matrix, composed of these row vectors. Note also that in order to compute the gradient of the penalty functional using eq. (14) we need to apply the operator

$$\left[\frac{\partial \psi}{\partial \mathbf{m}} \right]^H = \frac{\partial \rho}{\partial \mathbf{m}}^T \frac{\partial \mathbf{h}}{\partial \rho} \frac{\partial \psi}{\partial \mathbf{h}}^H \quad (17)$$

to the normalized residual vector.

3.2 Generalized forward problem with arbitrary forcing

The computation of $\partial \mathbf{h} / \partial \rho$ is the core of the sensitivity calculation. Suppose we introduce a small perturbation $\delta \rho$ into the Helmholtz eq. (4). Then, the perturbed equation

$$\nabla \times (\rho + \delta \rho) \nabla \times (\mathbf{H} + \delta \mathbf{H}) + i\omega\mu_0(\mathbf{H} + \delta \mathbf{H}) = 0 \quad (18)$$

can be linearized to obtain a system of equations for $\delta \mathbf{H}$,

$$\nabla \times \rho (\nabla \times \delta \mathbf{H}) + i\omega\mu_0 \delta \mathbf{H} = -\nabla \times \delta \rho (\nabla \times \mathbf{H}) \quad (19)$$

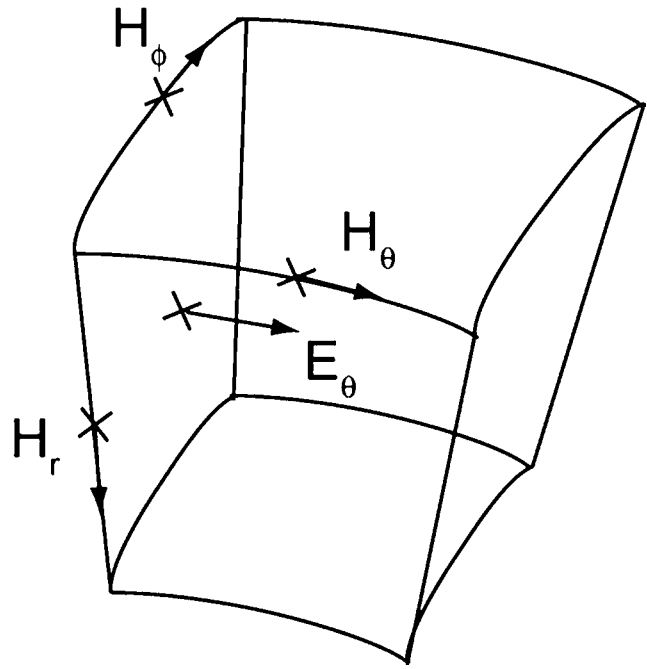


Figure 1. Spherical staggered-grid finite difference formulation: illustration of electric and magnetic field components in a single H -cell.

with homogeneous boundary conditions. Thus, to obtain $\delta \mathbf{H}$ (i.e. to calculate sensitivities) we need to solve the forward problem with a general interior source, which depends on the unperturbed magnetic field \mathbf{H} and on $\delta \rho$.

This requirement, together with the need to solve the adjoint system as part of the implementation of (17), suggests a more careful look at some details of the U&S numerical scheme.

3.3 Staggered-grid finite difference formulation, revisited

To discuss numerical computation of the derivatives in Section 3.1, it is necessary to refer to the staggered-grid discretization of U&S. Consider an H -cell bounded by H -faces (Fig. 1). The magnetic field components are defined on H -edges (edge centres). Electric fields are defined on H -faces (which correspond to the centres of E -edges). Length elements l_r , l_ϕ and l_θ are defined on H -edges. We can also define elementary areas S_r , S_ϕ and S_θ on both the H -faces and on the H -edges (which correspond to the E -faces). The latter are the areas of surfaces perpendicular to the H -edges, passing through their centres. We also define the (i, j, k) E -prism to be the prism centred at the (i, j, k) H -node, so that we can refer to (i, j, k) E -edges and E -faces in much the same way as those of H -prisms.

In the global spherical staggered-grid construction some components are undefined (such as the ϕ -components at the poles, or the radial components at the lower boundary of the domain) and some are redundant (such as the radial components at the poles). We consider the well-defined, ‘unique’ components in the centres, on the edges and on the surfaces of the H -prisms. To be more precise (and succinct) in description of the linear algebraic formulation of the discrete problem, we introduce the following finite-dimensional vector spaces:

$\mathbb{E} \equiv$ vector space of complex components defined on each unique H -edge on the grid.

$\mathbb{F} \equiv$ vector space of complex components defined on each unique H -face of the grid (or, equivalently, on each

unique E -edge, including those corresponding to the boundary surfaces).

$\mathbb{G} \equiv$ vector space of real components defined on the H -prisms.

To distinguish between interior and boundary components of the discrete field values we will use the subscripts \mathbf{i} (for interior) and \mathbf{b} (for boundary). Thus the full magnetic field vector can be represented as

$$\mathbf{h} = \begin{bmatrix} \mathbf{h}_i \\ \mathbf{h}_b \end{bmatrix}, \quad (20)$$

and \mathbb{E}_i and \mathbb{E}_b are complimentary subspaces of \mathbb{E} , consisting of interior and boundary edges, respectively.

As in U&S the boundary components are not solved for, and they may thus be eliminated from the system of discretized Maxwell's equations (eqs 18–19 of U&S) to yield

$$\mathbf{A}_{\rho,\omega} \mathbf{D}_l \mathbf{h}_i = -\mathbf{B}_\rho \mathbf{h}_b = -\mathbf{B}_\rho \mathbf{b}, \quad (21)$$

where \mathbf{D}_l is a diagonal operator which multiplies by the interior H -edge length elements, and $\mathbf{b} \in \mathbb{E}_b$ denotes the vector of boundary conditions (cf. eq. 20 in U&S). The RHS of the equation is defined by the mapping \mathbf{B}_ρ from the boundary H -edges of the grid to the interior H -edges. This mapping depends only on ρ and effectively produces a forcing on interior nodes from the specified boundary data. The operator $\mathbf{A}_{\rho,\omega} : \mathbb{E}_i \rightarrow \mathbb{E}_i$ is symmetric and real everywhere except along the diagonal, making it possible to solve the linear system of equations efficiently, using a variant of biconjugate gradients (Uyeshima & Schultz 2000; Toh *et al.* 2002).

3.4 Derivation of data sensitivities

The linearized relationship between a perturbation $\delta\rho$ in the model electrical resistivity and the respective perturbation $\delta\mathbf{h}_i$ in the magnetic field solution can be described by a discrete operator $\mathbf{J} : \mathbb{G} \rightarrow \mathbb{E}_i$, such that $\delta\mathbf{h}_i = \mathbf{J} \delta\rho$. Clearly, \mathbf{J} is an $|\mathbb{E}_i| \times |\mathbb{G}|$ matrix, where $|\cdot|$ denotes dimension of the space. To formally evaluate \mathbf{J} , consider the perturbed numerical forward solver,

$$\mathbf{A}_{\rho+\delta\rho,\omega} \mathbf{D}_l (\mathbf{h}_i + \delta\mathbf{h}_i) = -\mathbf{B}_{\rho+\delta\rho} \mathbf{b}, \quad (22)$$

and employ the identities (see the Appendix)

$$\mathbf{A}_{\rho+\delta\rho,\omega} = \mathbf{A}_{\rho,\omega} + \mathbf{A}_{\delta\rho,0} \quad (23)$$

and

$$\mathbf{B}_{\rho+\delta\rho} = \mathbf{B}_\rho + \mathbf{B}_{\delta\rho} \quad (24)$$

to obtain

$$\mathbf{A}_{\rho,\omega} \mathbf{D}_l \delta\mathbf{h}_i = -(\mathbf{A}_{\delta\rho,0} \mathbf{D}_l \mathbf{h}_i + \mathbf{B}_{\delta\rho} \mathbf{b}). \quad (25)$$

Note that the RHS depends linearly on $\delta\rho$. Therefore, it is possible to rewrite the system (25) as

$$\mathbf{A}_{\rho,\omega} \mathbf{D}_l \delta\mathbf{h}_i = -\mathbf{E}_h \delta\rho, \quad (26)$$

where $\mathbf{E}_h : \mathbb{G} \rightarrow \mathbb{E}_i$ is a complex linear operator that depends on \mathbf{h}_i . The derivation of operator \mathbf{E}_h is also found in the Appendix.

From (26), we obtain a formal expression for the Jacobian of the forward solver:

$$\mathbf{J} = \frac{\partial \mathbf{h}_i}{\partial \rho} = -\mathbf{D}_l^{-1} \mathbf{A}_{\rho,\omega}^{-1} \mathbf{E}_h. \quad (27)$$

We complete the setup with expressions for Jacobians of the model parametrization and the data functionals, namely, $\partial\rho/\partial\mathbf{m}$ and $\partial\psi/\partial\mathbf{h}_i$. Assuming data are only in the interior of the domain, data

functionals of interest all have the form $\psi_j(\mathbf{h}_i)$, where ψ_j is a simple (but non-linear) function of $\mathbf{h}_i \equiv \mathbf{h}_i(x_j)$, that is, the triplet (h_ϕ, h_θ, h_r) at $x_j = (\phi, \theta, r)$, the location of observation j . Note that ψ_j also depends on frequency. In general, we may write

$$\mathbf{h}_i(x_j) = L_j^T \mathbf{h}_i, \quad (28)$$

where L_j is a real sparse $|\mathbb{E}_i| \times 3$ matrix, that represents bilinear spline interpolation from the numerical grid (H -edges) to x_j . Decomposing the sparse matrix L_j as $L_j = (L_j^\phi, L_j^\theta, L_j^r)$, we have

$$\mathbf{g}_j^* = \frac{\partial \psi_j}{\partial \mathbf{h}_i} = \frac{\partial \psi_j}{\partial h_\phi} (L_j^\phi)^T + \frac{\partial \psi_j}{\partial h_\theta} (L_j^\theta)^T + \frac{\partial \psi_j}{\partial h_r} (L_j^r)^T. \quad (29)$$

For example, for the specific case of c response field ratios (cf. eq. 6),

$$\frac{\partial \psi_j}{\partial h_\phi} = 0, \quad \frac{\partial \psi_j}{\partial h_\theta} = -\frac{a}{2} \frac{h_r}{h_\theta^2}, \quad \frac{\partial \psi_j}{\partial h_r} = \frac{a}{2} \frac{1}{h_\theta} \quad (30)$$

are used in (29), with the magnetic field (h_ϕ, h_θ, h_r) calculated using (28).

Finally, define $\mathbf{P} : \mathbb{R}^M \rightarrow \mathbb{G}$ through the linear relation $\delta\rho = \mathbf{P} \delta\mathbf{m}$ and set $\hat{\mathbf{P}} = \mathbf{P} \mathbf{C}_m^{1/2}$ so that $\delta\rho = \hat{\mathbf{P}} \delta\hat{\mathbf{m}}$. For parametrization in the form

$$\log_{10} \rho(\phi, \theta, r) = \sum_{i=1}^M m_i f_i(\phi, \theta, r) \quad (31)$$

for some set of basis functions f_i and coefficients m_i , for the prism centred at (ϕ, θ, r) , the corresponding components of the operator \mathbf{P} are

$$p_i(\phi, \theta, r) = \frac{\partial \rho}{\partial m_i}(\phi, \theta, r) = \rho(\phi, \theta, r) f_i(\phi, \theta, r) \ln(10). \quad (32)$$

By denoting by $\psi(\mathbf{m})$ the $N_\omega \times 1$ vector with components $\psi_j(\mathbf{m})$ for all sites and for a fixed frequency ω , and letting \mathbf{G}_ω be the $|\mathbb{E}_i| \times N_\omega$ complex matrix whose j th column is \mathbf{g}_j^* , the full Jacobian of the mapping from model parameters to data for frequency ω may then be expressed as

$$\frac{\partial \psi}{\partial \hat{\mathbf{m}}} = \mathbf{G}_\omega^* \hat{\mathbf{J}} \hat{\mathbf{P}}, \quad (33)$$

where \mathbf{J} is given by eq. (27).

3.5 Direct and adjoint approaches

Denoting the vector of weighted residuals as

$$\tilde{\mathbf{r}}_\omega = \mathbf{C}_d^{-1} [\psi_\omega(\mathbf{m}) - \mathbf{d}]. \quad (34)$$

the discrete equivalent of the adjoint gradient expression (14) is

$$\left[\frac{\partial R_\omega}{\partial \hat{\mathbf{m}}} \right]^T = 2 \operatorname{Re} (\hat{\mathbf{P}}^T \mathbf{J}^* \mathbf{G}_\omega \tilde{\mathbf{r}}_\omega) + 2\lambda \hat{\mathbf{m}}. \quad (35)$$

To evaluate (35) we only need to perform the forward computations twice for every frequency: once with the direct forward solver to evaluate \mathbf{h} , and a second time with the adjoint solver to implement $\mathbf{J}^* \mathbf{G}_\omega \tilde{\mathbf{r}}_\omega$ and evaluate the derivative.

The adjoint computations involve solving a slightly different system of equations, which requires only minimal modifications to the original system. Indeed, since inversion and conjugation may be freely interchanged for finite-dimensional linear operators,

$$\mathbf{J}^* = -\mathbf{E}_h^* (\mathbf{A}_{\rho,\omega}^*)^{-1} \mathbf{D}_l^{-1}. \quad (36)$$

The only complex components of $\mathbf{A}_{\rho,\omega}$ are due to the $-i\omega\mu_0$ term on the diagonal. We use

$$\mathbf{A}_{\rho,\omega}^* = \mathbf{A}_{\rho,-\omega} \quad (37)$$

to obtain

$$\mathbf{J}^* = -\mathbf{F}_h^* \mathbf{A}_{\rho, -\omega}^{-1} \mathbf{D}_l^{-1}. \quad (38)$$

Then, evaluation of the derivative in the adjoint formulation requires solving the linear system

$$\mathbf{A}_{\rho, -\omega} \tilde{\mathbf{h}}_i = \mathbf{D}_l^{-1} \tilde{\mathbf{f}} \quad (39)$$

for $\tilde{\mathbf{h}}_i$, where $\tilde{\mathbf{f}} = \mathbf{G}_\omega \tilde{\mathbf{r}}_\omega$.

Thus, the discrete adjoint corresponds to a variant of the system of eq. (21) for the forward problem. Furthermore, the core numerical forward solution developed by U&S may be used, with relatively minor modifications (Appendix, Section A5), to solve the adjoint system. The adjoint approach allows us to evaluate the derivative at the cost of a single run of the forward solver, independent of the complexity of the model space. This allows us to consider far more detailed parametrizations than would be practical with a direct approach.

4 SYNTHETIC DATA EXPERIMENTS

We demonstrate the convergence and resolution of the conjugate gradient inverse solver based on the adjoint method (Sections 2.5 and 3.5) on a series of synthetic data examples.

The logarithmic resistivity perturbation is modelled as a spherical harmonic expansion in geomagnetic coordinates with 12 layers. Only the upper eight mantle layers are allowed to be heterogeneous, while the four layers from 1600 km depth to the CMB are assumed to be homogeneous, but free to vary. This assumption is justified by the fact that deeper structures, if present, cannot be easily resolved with external EM induction methods due to contamination by secular variations of the Earth's main field. The layer boundaries are defined to allow stronger radial variations in electrical resistivity in the upper to mid-mantle, and to accommodate the standard mantle discontinuities. We invert for the 3-D perturbations around the prior 1-D structure (Fig. 2).

The synthetic data, comprised of c and d response ratios (Section 2.3), is designed to resemble the global observatory data set compiled by Fujii & Schultz (2002) (henceforth F&S) in terms of the observatory distribution and frequency range, as well as in terms of the measurement errors. The effects of these on the resolution of the model at various depths is studied by varying each of these factors in turn and computing independent inverse solutions for each case.

While issues related to source field approximation certainly require attention, they are beyond the scope of this work. We eliminate

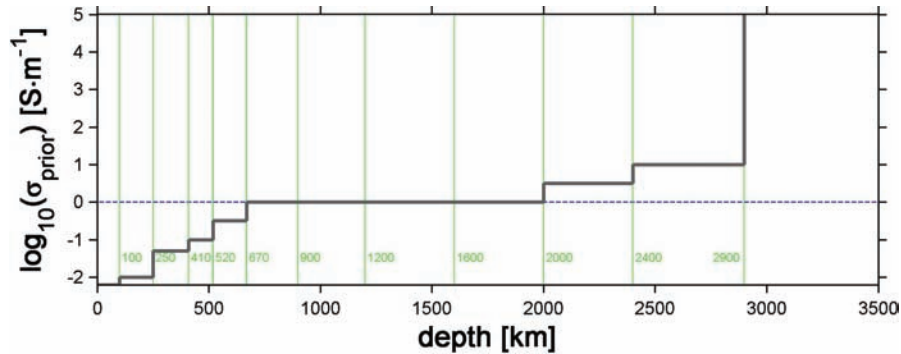


Figure 2. The prior model used for the synthetic inversions is based on Kuvshinov & Olsen (2006). The green vertical lines indicate layer boundaries for the model parametrization in km. A 12.65 km sheet of averaged near-surface conductance is included in the prior unless otherwise specified.

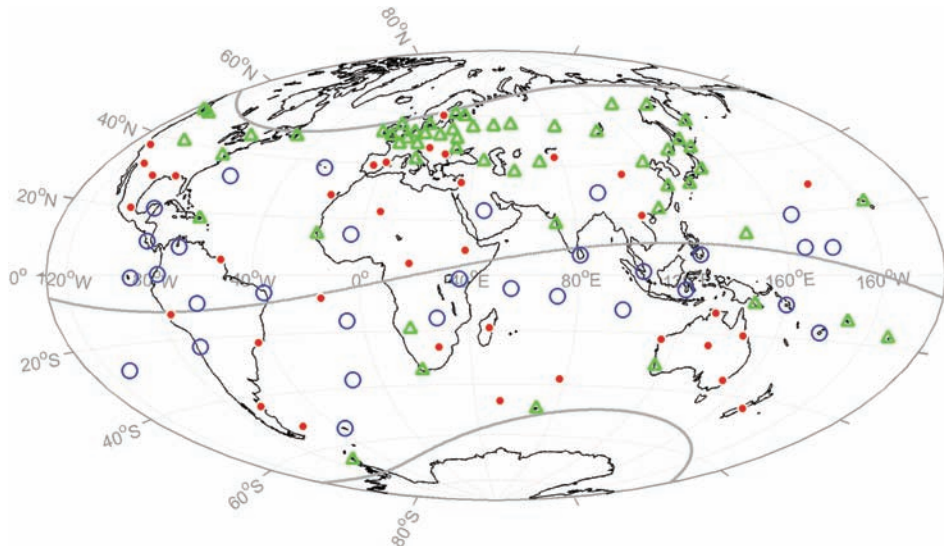


Figure 3. Mid-latitude ($-60^\circ \leq \theta \leq 60^\circ$) observatory locations used for synthetic data generation (127 in total). The green triangles are the 54 Fujii & Schultz (2002) geomagnetic observatory locations. The red solid dots are the 35 IAGA geomagnetic observatory locations as of 2006 July, distinct from the F&S observatories. The blue open circles denote a set of 38 IRIS GSN observatory locations as of 2006 October that are over 1100 km away from any of the existing geomagnetic observatories and from each other.

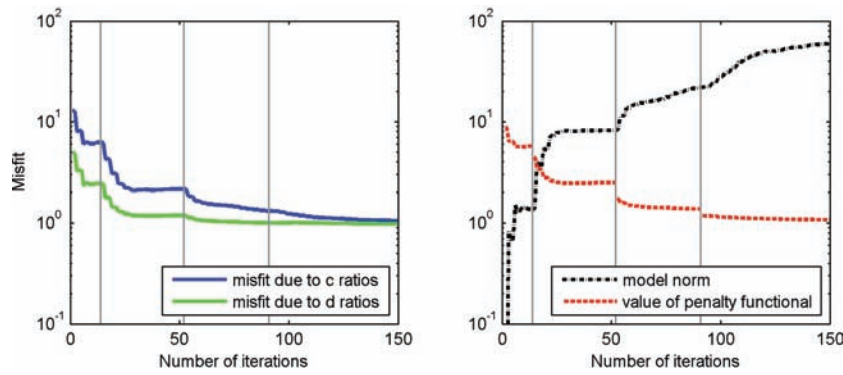


Figure 4. Example convergence rate, plotted for the synthetic inversion reconstructing degree 5 order 3 conductivity perturbation in layer 6 using synthetic data at $\text{REG24} \times 16$ locations. The left-hand plot shows the misfits due to c and d ratios, respectively. The right-hand plot shows the corresponding model norm (black) before weighting by the damping parameter. The dashed red line corresponds to the total value of the penalty functional, which is the sum of the model norm (weighted by the damping parameter λ) and the averaged misfit. The solid vertical lines denote the points at which the damping parameter has been updated. Note that at these points the penalty functional is effectively redefined, and so the plotted curve is discontinuous.

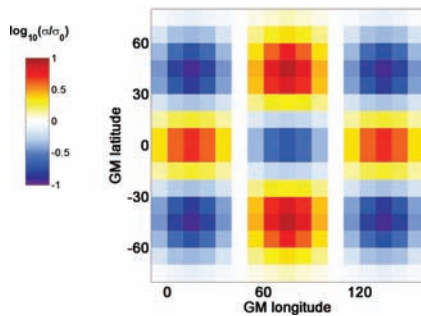


Figure 5. Synthetic degree 5 order 3 checkerboard model in geomagnetic coordinates plotted for comparison with the resolution kernels in Figs 6–8, with the same scaling and projection. Note that only one hemisphere is plotted.

additional complications arising from the unknown source field structure by both generating the synthetic data and inverting it under the assumption of a P_1^0 source. This assumption clearly breaks down at higher latitudes (see, for example, F&S's method of assimilating higher-latitude data influenced strongly by the auroral conjugate current systems). For the present examples, we deal with the issue more simply, by restricting attention to mid-latitude observatory distribution, with latitudes not higher than $\pm 60^\circ$ geomagnetic.

Fig. 3 presents three of the four global observatory distributions used for the generation of synthetic data: the F&S mid-latitude observatories (54 locations), the F&S data set combined with the additional mid-latitude INTERMAGNET (joint effort of IAGA and IUGG Coles *et al.* 1990) observatories as of 2006 July (89 locations), and both sets combined with an additional 38 hypothetical geomagnetic observatory locations. These correspond to a set of primarily island based IRIS global broad band seismometers, providing geographical coverage in areas distant from any existing geomagnetic observatory, and bringing the total to 127 locations. Additionally, we also consider an even more hypothetical regular grid of observatories located between -56° and 56° geomagnetic latitude, with the latitudinal distance between the adjacent locations being 16° and longitudinal 24° , starting from zero geomagnetic longitude (120 locations in total). Henceforth, we shall refer to these observatory distributions as F&S, F&S+IAGA, F&S+IAGA+GSN and $\text{REG24} \times 16$, respectively.

In order to obtain more realistic errors in the synthetic data, we have performed a linear regression analysis of the F&S absolute data errors, converted to the errors δ_r in the field ratios of (6) and (7). The two parameter model

$$\delta_r = \beta_0 + \beta_1 \tan \left| \frac{\pi}{2} - \theta \right|, \quad 0 < \theta < \pi, \quad (40)$$

fits the data adequately for a range of frequencies, with the R^2 statistic approximately 0.8. For the field data, both regression coefficients span the range 30–100 km, depending on the frequency and the range of latitudes considered; in general, errors in c ratios increase more rapidly with latitude than the errors in the d ratios. The realistic averaged values of these parameters for the frequency range of F&S (periods of ~ 5 –106 d) are approximately $\beta_0 = 60$ km, $\beta_1 = 80$ km for the c ratios, and $\beta_0 = 50$ km, $\beta_1 = 30$ km for the d ratios. These are the values we have used in our synthetic experiments. For some experiments, we model hypothetical data of better quality using the value of $\beta_0 = 10$ km for both types of responses.

The resolution analysis performed in this paper was based on inversions of both c and d field ratios. This choice was justified by comparison of the quality of the inverse solutions obtained with the c ratio data only to that of the solutions computed using both c and d ratios. The inverse solutions obtained with the mixed data set exhibit better resolved anomalies with sharper boundaries.

Most of the experiments described below have been performed with a $36 \times 18 \times 52$ grid, including seven air layers. This corresponds to $10^\circ \times 10^\circ$ in tangential directions. This grid size is sufficient to model the large-scale mantle inhomogeneities considered in this paper, and at the same time is computationally tractable. The near-surface conductance, associated with the oceans and marine and terrestrial sedimentary cover, has been averaged to the same grid. The inversions were performed using the same grid and the same vertical layering as those used for preparation of the synthetic data, unless otherwise specified.

Tests were first performed to assess the sensitivity of the inverse solution to this near-surface conductance. Synthetic data were generated on the $\text{REG24} \times 16$ observatory grid for a degree 5 order 3 checkerboard perturbation in the upper mantle (12.65–670 km depths), with the near-surface S-map above 12.65 km depth superimposed. A random distortion of amplitude 20 per cent in the $10^\circ \times 10^\circ$ S-map was then generated, and this was imposed as a fixed surface conductance in the inversion of the synthetic data. The

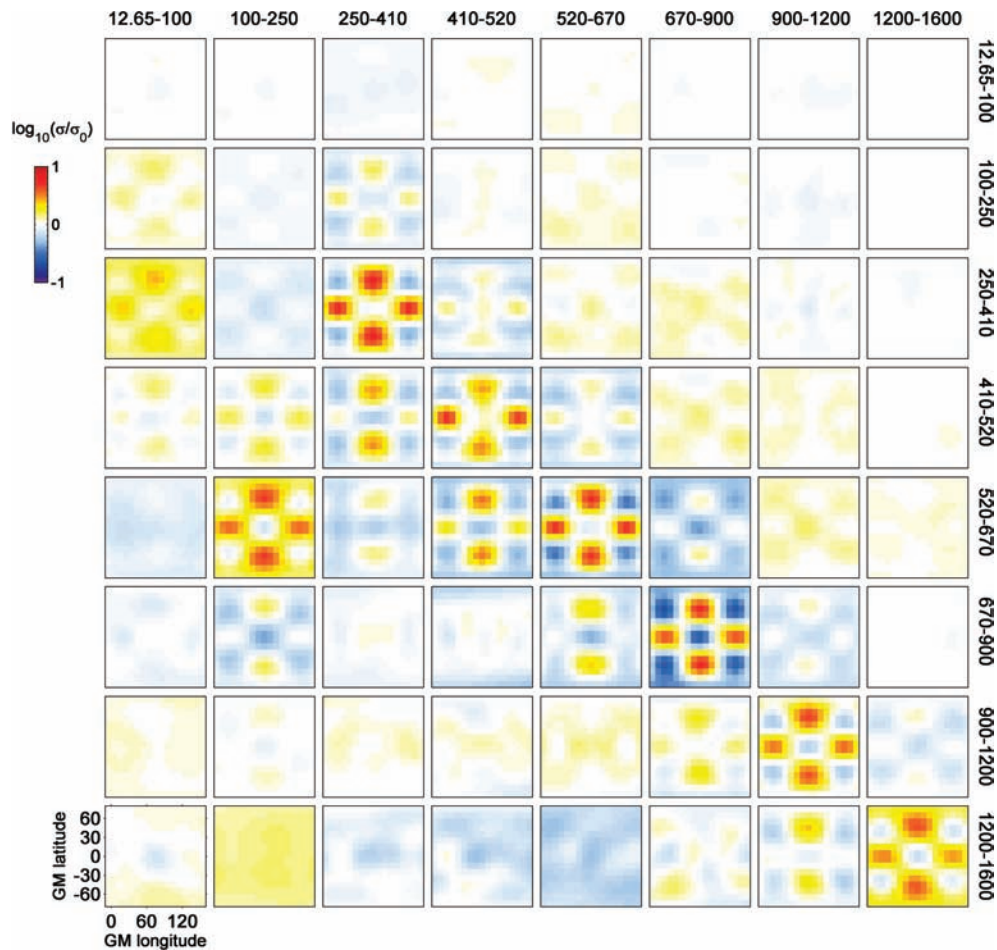


Figure 6. The resolution kernel for degree 5 order 3 conductivity perturbation on a single layer. Each column k corresponds to a single inverse model, obtained by reconstructing the perturbation on layer k . The solutions were obtained with both horizontal and vertical smoothing and with 13 sample periods in the range 5.12–107 d.

error introduced into the inverse model solution by using the incorrect surface conductance was found insignificant for the frequency range of the F&S data. However, the inverse solution obtained with the surface conductance totally omitted from the inversion has a notably more conductive upper mantle above ≈ 410 km depth, particularly below the oceans. The S-map has thus been included, but assumed to be correct, in all of the examples discussed below.

5 RESULTS

5.1 Vertical resolution

The vertical resolution of the conjugate gradient inverse solution has been tested by a series of computational experiments with idealized data. Synthetic c and d responses were generated on the REG24 \times 16 grid for eight models, corresponding to a degree 5 order 3 checkerboard perturbation around the prior model (Fig. 2) within each of the eight uppermost layers (12.65–1600 km). To specifically address the issue of vertical resolution, we inverted unrealistically accurate data with least-squares fitting parameters of expression (40) adjusted to $\beta_0 = 10$, $\beta_1 = 80$ for c ratios and $\beta_0 = 10$, $\beta_1 = 30$ for d ratios. For inversion, we assumed a degree and order 6 parametrization in the top eight layers above 1600 km, with 1-D structure below this

depth. The inversions were regularized by smoothing as described in Section 2.4, with the smoothing parameter values $\alpha = 0.5$, $\beta = 0.8$.

Plotted in Fig. 4 is a typical rate of convergence of a synthetic inversion based on degree and order 6 spherical harmonic parametrization. In this case, the total number of variable parameters is 396, corresponding to 49 parameters for each of the eight heterogeneous layers and a single parameter for each of the four homogeneous layers. In this example, as well as in other examples discussed in this paper, the starting value of the damping parameter was set to 1. The damping parameter was updated ($\lambda \rightarrow \lambda/10$) when the norm of the gradient of the penalty functional decreased to 0.01 of its initial value. The procedure was stopped when the averaged misfit was close enough to 1. The number of function (and derivative) evaluations per line search was set to 3, and a full inversion typically required an order of 50 line searches.

The results of these inversions for 13 sample frequencies spaced evenly within the F&S period range (5.12–107-d periods) are presented in Fig. 6. Here, each column corresponds to the upper eight layers of the inverse solution for each of the eight test cases, so the 8×8 matrix of subplots can be viewed effectively as a vertical resolution matrix, for the large-scale checkerboard perturbation of Fig. 5. For clarity of presentation, the perturbations around the prior in the synthetic model and in the inverse solutions are divided by

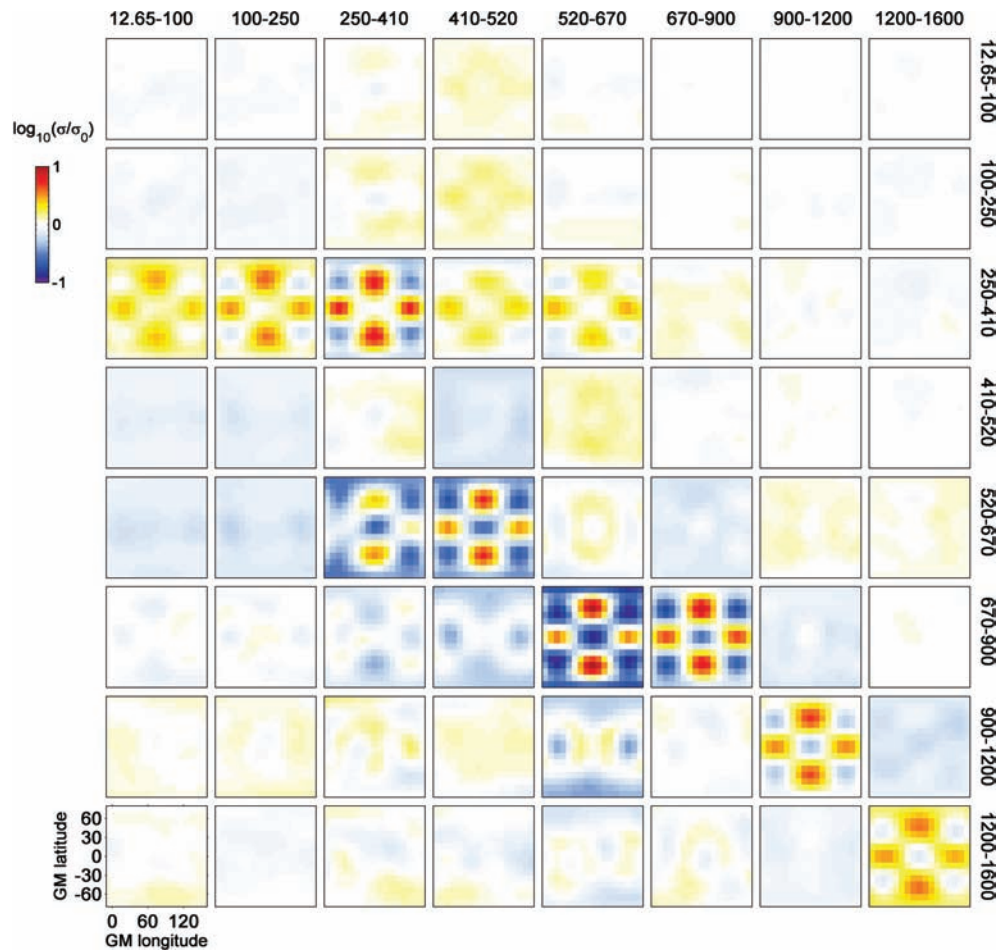


Figure 7. The resolution kernel for degree 5 order 3 conductivity perturbation on a single layer. Each column k corresponds to a single inverse model, obtained by reconstructing the perturbation on layer k . The solutions were obtained without the vertical smoothing and with 13 sample periods in the range 5.12–107 d.

the magnitude of the synthetic perturbation (± 2.5 in $\log_{10}\rho$) and plotted in the range $[-1, 1]$. We plot only the section of the model corresponding to one hemisphere (due to the longitudinal symmetry of the checkerboard model, results for the other hemisphere are identical).

Fig. 6 indicates that the spatial resolution of these large-scale features is very good (compare with the synthetic structure in Fig. 5) from the bottom of the transition zone into the lower mantle to a depth of about 1600 km. At these depths the inverse solution conductivity has a well defined peak in the correct layer. For perturbations in the transition zone, peaks are more poorly defined in the inverse solutions. In the upper-mantle resolution becomes very poor.

In Fig. 7, we consider inversions of the same limited frequency data set, but now with vertical smoothing turned off in the model covariance (that is with $\beta = 1.0$). Without the vertical smoothing the solutions become erratic, with peaks misplaced for perturbations in all layers above the top of the lower mantle. Although the smoothing does smear the conductivity vertically, comparison of Figs 6 and 7 shows clearly that vertical smoothing is justified.

In Fig. 8, we plot the results of vertically smoothed resolution experiments with synthetic data covering a broader range of periods (14 bands, with periods sampled regularly from 0.2 to 107 d). This expanded period range would correspond to including daily variation data in the inversion. Although in practice such shorter period data would be dominated by shorter wavelength non-zonal iono-

spheric source fields, for purposes of our synthetic data experiment we retain the P_1^0 source approximation. As Fig. 8 shows, inclusion of such shorter period data would provide reasonably good resolution of large-scale features throughout the upper mantle.

5.2 Horizontal spatial resolution

To assess the effect of the horizontal distribution of the data on resolution we first consider, as in Section 5.1, a degree 5 order 3 checkerboard perturbation in the shallowest well-resolved layer (670–900 km), and attempt to reconstruct it with data in the period range 5.12–107 d for different observatory distributions. We also consider a degree 8 order 4 checkerboard perturbation on the same layer, to see how the spatial distribution of the data affects the resolution of these slightly finer features. The two synthetic models are shown at the top of Fig. 9. These experiments have been performed with the smoothing parameters $\alpha = 0.5$, $\beta = 0.8$. To test both the fidelity of the model reconstruction and the efficiency of the regularization, we overparametrize the models. The degree 5 order 3 synthetic example has been inverted with degree and order 6 parametrization, while the degree 8 order 4 example used a degree and order 9 parametrization in the inversion. In this experiment, as opposed to the vertical resolution test in Section 5.1, we inverted data with a realistic noise level similar to that in the F&S data set

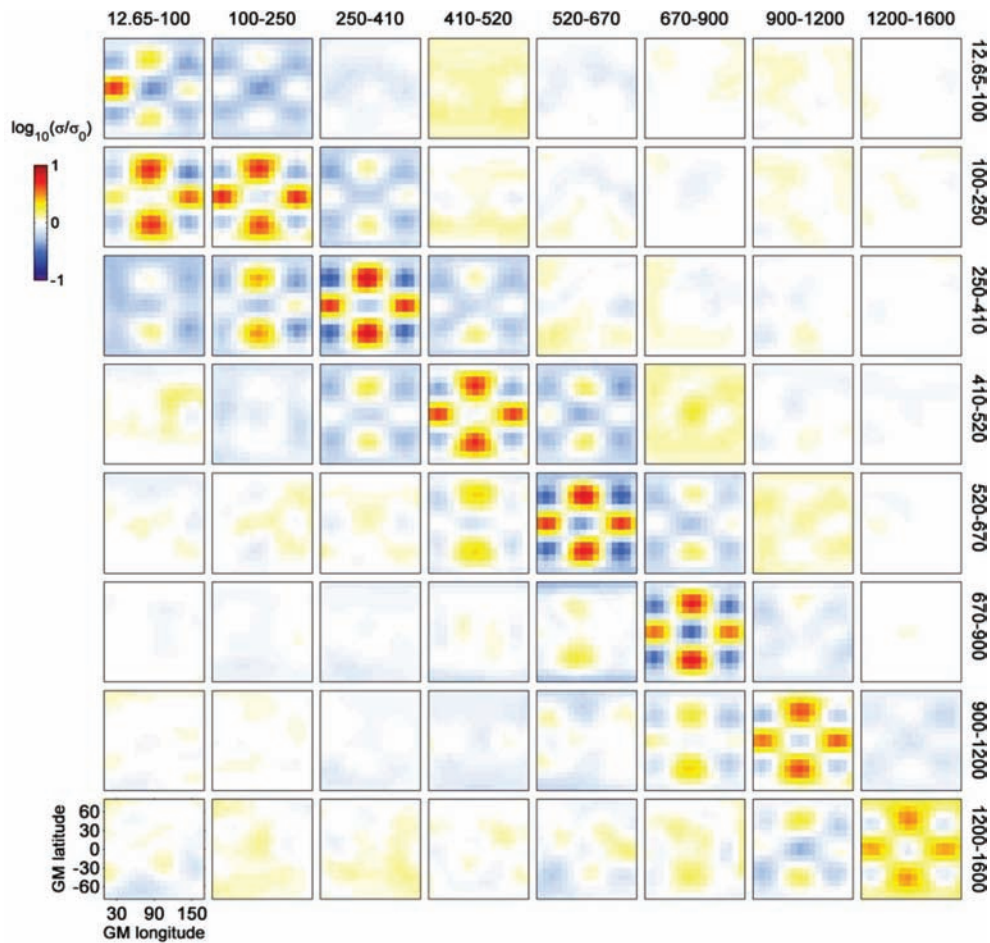


Figure 8. The resolution kernel for degree 5 order 3 conductivity perturbation on a single layer. Each column k corresponds to a single inverse model, obtained by reconstructing the perturbation on layer k . The solutions were obtained with both horizontal and vertical smoothing and with 14 sample periods in the range 0.2–107 d.

(regression parameters $\beta_0 = 60$ km, $\beta_1 = 80$ km for the c ratios, and $\beta_0 = 50$ km, $\beta_1 = 30$ km for the d ratios).

Fig. 9 presents the inverse solutions obtained with the REG24×16, F&S+IAGA and F&S data distributions versus the respective synthetic models. Only the target layer (670–900 km) in the inverse solution is shown. To give an idea of the leakage of the anomalies into the neighbouring layers, we also plot the total conductance for the target layer and the layers above and below (520–1600 km) in Fig. 10.

It is immediately notable from the degree 5 order 3 inverse solution obtained by inverting the REG24×16 data distribution (Fig. 9) that the amplitude of the perturbation is approximately half the size of the synthetic used to generate the data. This was not the case in the vertical resolution experiments, performed with unrealistically small data errors. Thus we conclude that unless the data quality is improved the inversion does not fully recover the magnitudes of the anomalies in the target layer. However, comparison of Fig. 9 with the total conductance plotted in Fig. 10 shows that the reduction in amplitude is largely due to vertical smearing of the conductivity into adjacent layers.

It is instructive to compare the results obtained with different data distributions. We note that areas with large gaps in observatory coverage (such as the southern hemisphere, particularly beneath South America, in the F&S distribution of observatories) have

weak anomalies in the inverse solutions. Not surprisingly, this becomes even more of an issue for shorter spatial scale features. Some smaller anomalies in the areas of poor observatory coverage tend to get aliased to large-scale features in the data gap (such as the positive anomalies beneath North Australia and off the east coast of the Americas); others are missed (such as the anomalies beneath South America, Northwest Africa and everything south of Australia).

The discussion above relies on the assumption that the vertical resolution does not depend a great deal upon the observatory coverage. We explore this issue further by plotting the inverse solutions as a function of depth in the spherical harmonic domain for different observatory distributions (Fig. 11). It can be seen that the magnitude of the reconstructed perturbation increases with better geographic data coverage, going from ~30 per cent of the synthetic perturbation to ~60 per cent, while the total error decreases in both the target layer and the deeper layers. Thus, geographic data coverage is another factor influencing vertical resolution and the propagation of errors to deeper layers.

We conclude that potentially important large-scale features near the top of the upper mantle will be missed in the areas of poor data coverage; however, in areas where the observatory data are available, such features should be laterally resolved, even with a sparse and irregular global data set such as F&S (see e.g. Fig. 9). If all of the current INTERMAGNET observatories were added to

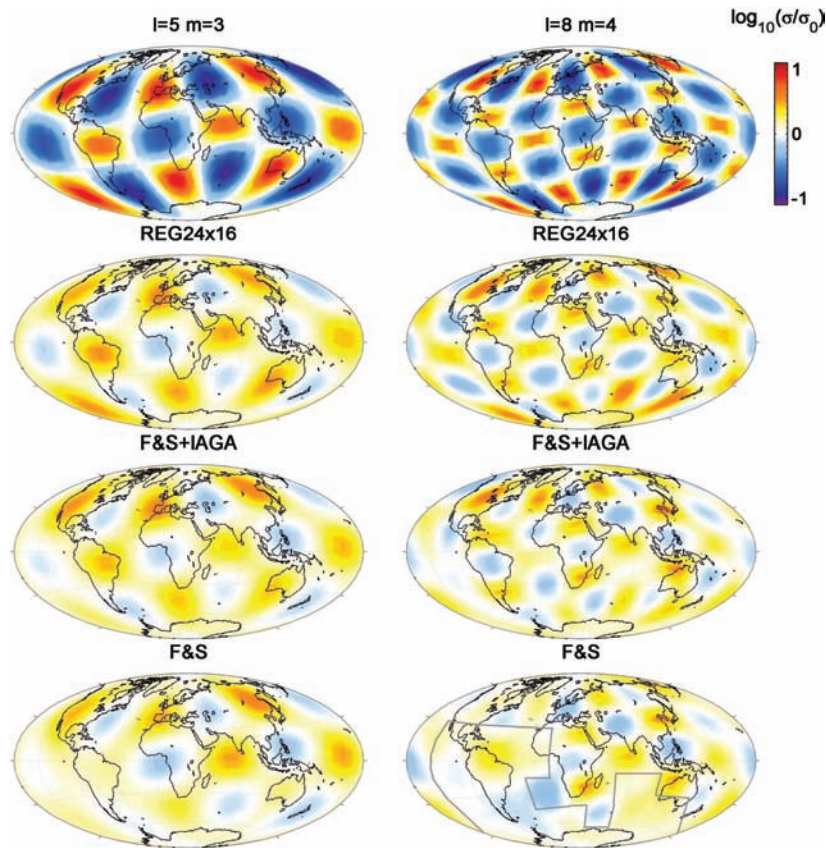


Figure 9. Inverse solutions for a range of data distributions REG24×16, F&S+IAGA and F&S (as described in Section 4) compared to the checkerboard parametrizations degree 5 order 3 (column 1) and degree 8 order 4 (column 2) on the target layer 670–900 km depth. The region above the grey borderline in the bottom right-hand figure contains the anomalies that are reasonably well-resolved, although underestimated, with the F&S data and error distribution.

this set (F&S+IAGA), a number of gaps, especially in the southern hemisphere, would be filled in.

5.3 A more realistic example based on the SPRD6 shear wave velocity model

To construct a more realistic synthetic example, we start with the Ishii & Tromp (2001) shear wave velocity model, based on seismic normal-mode data and the geoid. This model is parametrized with spherical harmonics to degree and order 6 with Chebyshev polynomials in the vertical. We mapped this to a layered model after rotation of the spherical harmonic coefficients to geomagnetic coordinates using a Wigner D-matrix (Hillery *et al.* 1984). The coefficients in the upper eight layers of the model (with layers defined as in Fig. 2) were then rescaled to correspond to perturbations in log-conductivity via

$$\log_{10} \left(\frac{\rho}{\rho_0} \right) = v_s \sqrt{d}/10, \quad (41)$$

where d is the mid-layer depth in metres. The scaling in (41) was chosen to make the amplitude of the perturbations realistic, in the sense that the deviation from spherical symmetry in the c responses resulting from this perturbation is comparable to that seen in the F&S data set. Below 1600 km depth the mantle has been parametrized with a 1-D layer structure. Near-surface electrical conductivity is included as in the checkerboard tests.

The synthetic model was then perturbed by finer scale random features (up to degree and order 14 spherical harmonics) and syn-

thetic data were generated by solving the forward problem on $10^\circ \times 5^\circ$ grid. The synthetic models, with and without the random higher order perturbation, are shown in the first two columns of Fig. 12. The period range for these experiments was as in F&S, and observatory distributions, and data errors were as described in Section 4. Fig. 12 (columns 3 and 4) shows the reconstructed perturbations around the prior, obtained with a restricted degree and order 6 parametrization with vertical and horizontal smoothing ($\alpha = 0.5$, $\beta = 0.8$). Computations for the inversion were done on the coarse $10^\circ \times 10^\circ$ grid. By comparing the last three columns in Fig. 12 we see that the large-scale features of the synthetic model are reasonably well reconstructed at the mid-mantle depths (just where vertical resolution was reasonably good, Fig. 6) even with the irregular and sparse observatory distribution of F&S. The additional observatories from the F&S+IAGA+GSN have relatively minor impact on the inverse solution at the top of the upper mantle, although they do improve resolution of smaller scale features at all depths, and yield a substantially more accurate reconstruction in mid- to lower mantle. In spite of the presence of smaller scale conductivity perturbations of substantial amplitude in the synthetic model used to generate the data, the inversion reproduced the underlying large-scale features reasonably well.

6 CONCLUSIONS

An adjoint NLCG inversion technique for global EM has been developed and implemented. This technique is computationally tractable at the modest resolution justified by the sparse observatory

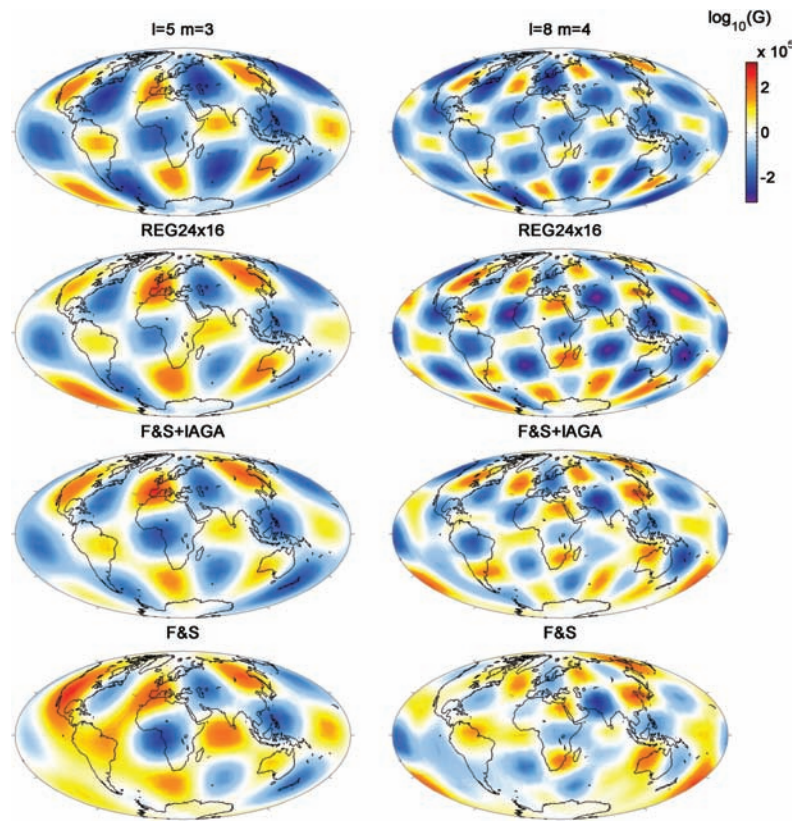


Figure 10. Conductance G (Siemens) for the depths 520–1600 plotted on the logarithmic scale. The inverse solutions obtained with the data distributions REG24 \times 16, F&S+IAGA and F&S are compared to the conductance of the respective checkerboard (670–900 km) parametrizations degree 5 order 3 (column 1) and degree 8 order 4 (column 2).

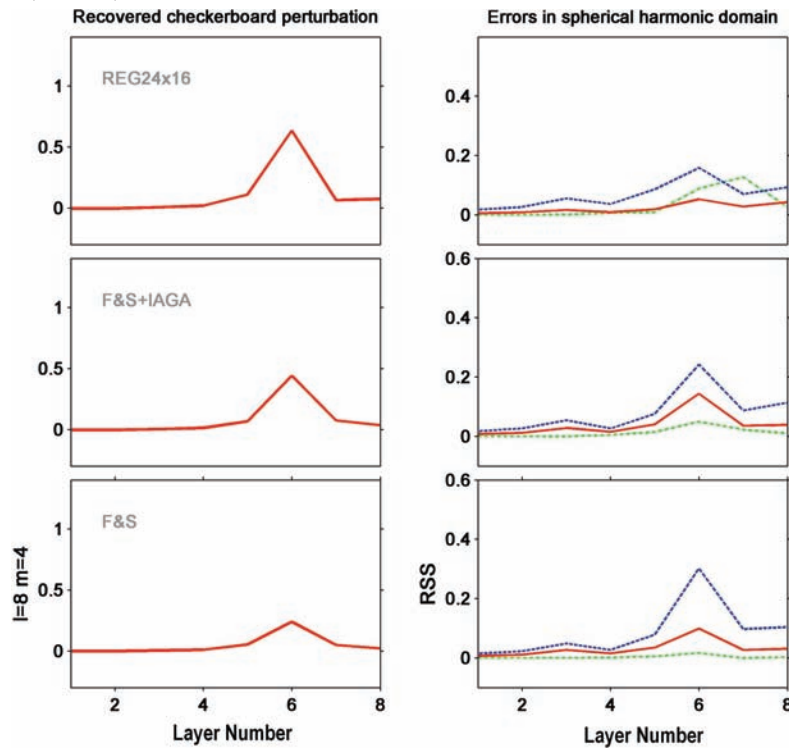


Figure 11. Inverse solutions for a range of data distributions REG24 \times 16, F&S+IAGA and F&S for the degree 8 order 4 checkerboard parametrization. The solid red line in the left-hand figure indicated the resolved degree $l = 8 \ m = 4$ spherical harmonic coefficient versus layer number. The red line in the right-hand figure corresponds to the root sum of squares of the erroneously resolved coefficients of the same degree. The dashed green line shows the zero degree and order coefficient. The dashed blue line shows the root sum of squares of the erroneous coefficients for $l \neq 8$. Ideally, the recovered perturbation would be 1 in layer 6 and zero otherwise.

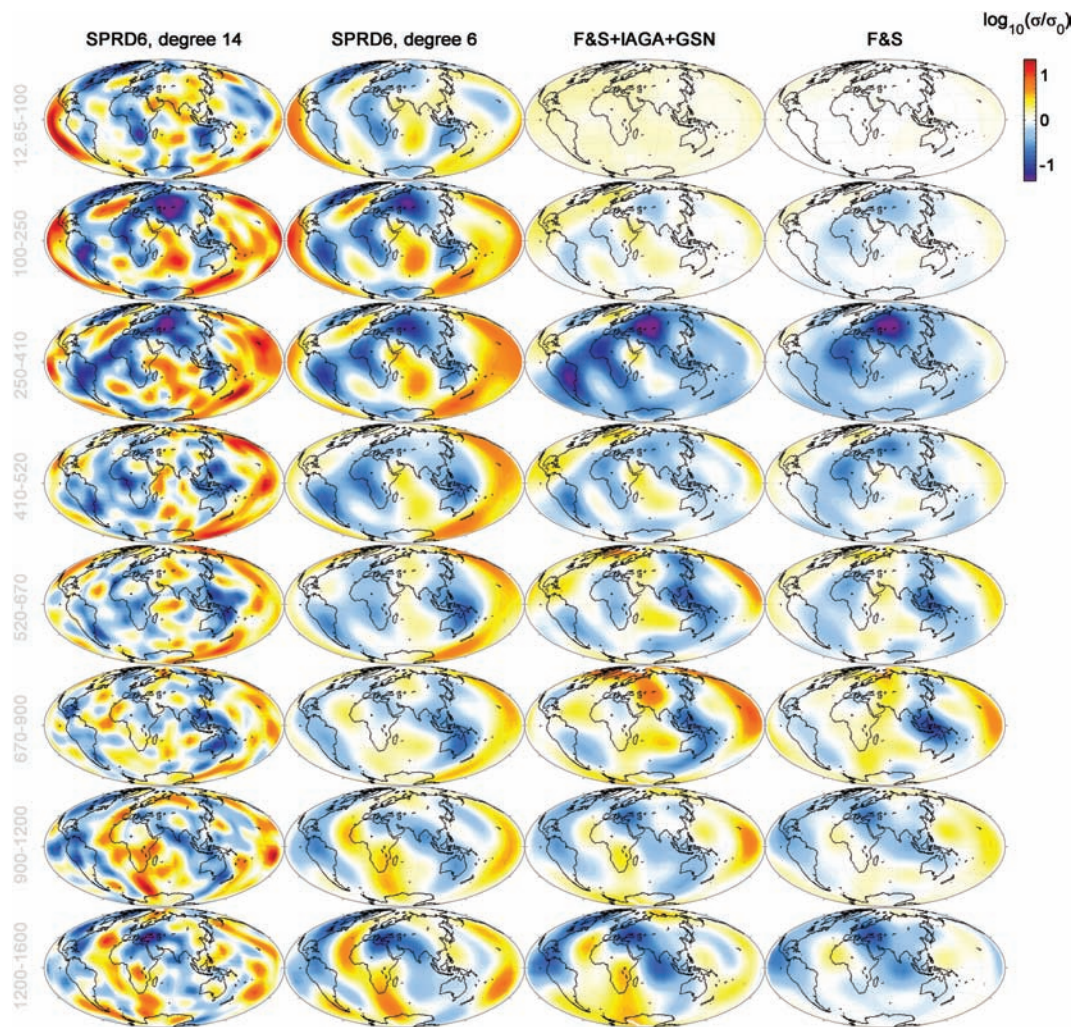


Figure 12. Two inverse solutions (columns 3 and 4) obtained by reconstructing the rescaled and randomly perturbed Ishii & Tromp (2001) SPRD6 *S*-wave model (column 1), using a degree and order 6 parametrization and observatory distributions F&S+IAGA+GSN and F&S. The corresponding rescaled degree and order 6 SPRD6 model is also shown (column 2). Only deviations from the prior are plotted. The inverse models fit the corresponding synthetic data sets with rms values of approximately 1.09 for *c* response ratios and 1.00 for *d* response ratios.

coverage: an inversion requires 2–3 d on a typical desktop workstation to complete. An extensive resolution analysis of the method has been performed.

The experiments described in Section 5.1 suggest that increasing the frequency bandwidth of the observatory depth soundings to include periods in the daily variations band yields a very substantial improvement in resolution of upper-mantle conductivity structure. Getting reliable response functions at these shorter periods will be a challenge, because source structure is much more complex and variable in time. However, there are good reasons to suppose that lateral variations in upper-mantle conductivity might be substantial (e.g. Xu *et al.* 1998; Toffelmier & Tyburczy 2007), so serious effort to obtain more reliable estimates of induction responses at these periods is well justified.

We have shown in Section 5.2, that the observatory distribution and period range of Fujii & Schultz (2002) resolves large-scale (few thousand kilometres) conductivity variations, from the lower part of the transition zone to ~1600 km depth. Vertical resolution length scales in this depth range are 300–500 km. In areas of the globe where the data distribution is sparse (in the ocean basins, and the southern hemisphere) features are washed out, or aliased to

larger scale structures. Our results reveal the geographical regions in which the resolution of data sets similar to F&S is best, and those in which the resolution is poor. This knowledge will be of use to those interpreting inversions of magnetic observatory data sets, and to those planning future observatory installations in remote areas.

By including a larger set of recently occupied INTERMAGNET observatories both vertical and horizontal resolution is enhanced, especially in areas such as South America, where the F&S data set is particularly deficient. Additional, but at this time hypothetical, observatories in the locations of 38 mostly island-based broad band seismic observatories would result in modest further improvements in resolution. Gains would probably be even greater at shorter wavelengths, which we did not investigate here.

In synthetic model experiments with shorter spatial wavelength conductivity perturbations added (Section 5.3), large-scale structure is still recovered with reasonable accuracy, giving confidence that large-scale structure in the Earth may be recovered even with the rather sparse data sets that are presently available. This gives at least some confidence that inversion of data sets such as that of F&S, and extensions, can reveal at least large-scale variations in conductivity near the bottom of the transition zone and top of the lower mantle.

ACKNOWLEDGMENTS

The authors are grateful to Dmitry Khmelev for his immense help in designing the inverse solver object communications. The authors thank Alexei Kuvshinov for his map of near-surface conductance. We are grateful to him, and to the anonymous reviewer, for their careful reading that helped improve the clarity of the paper. The authors also thank I. Fujii for providing the digital pre-processed global observatory responses, and F. J. Simons for making his Matlab code for rotation of spherical harmonic coefficients publicly available online. The authors acknowledge the UK Natural Environment Research Council EMS programme for its support of A. Kelbert's PhD studentship, the National Science Foundation grant 0345438-EAR for support of G. Egbert and the NSF Ocean Science Division for support of A. Schultz. The views expressed in this paper are those of the authors, and do not necessarily represent the views of the National Science Foundation.

REFERENCES

- Bahr, K., Olsen, N. & Shankland, T.J., 1993. On the combination of the magnetotelluric and the geomagnetic depth sounding method for resolving an electrical conductivity increase at 400 km depth, *Geophys. Res. Lett.*, **20**, 2937–2940.
- Banks, R., 1969. Geomagnetic variations and the electrical conductivity of the upper mantle, *Geophys. J. R. astr. Soc.*, **17**, 457–487.
- Banks, R.J. & Ainsworth, J.N., 1992. Global induction and the spatial structure of mid-latitude geomagnetic variations, *Geophys. J. Int.*, **110**, 251–266.
- Boehler, R., 1996. Melting temperature of the Earth's mantle and core: Earth's thermal structure, *Annu. Rev. Earth Planet. Sci.*, **24**(7), 15–40.
- Coles, R.L., Green, A.W. Jr., Lemouel, J.-L. & Stuart, W.F., 1990. Inter-magnet, in *Finnish Meteorological Inst., Proceedings of the International Workshop on Geomagnetic Observatory Data Acquisition and Processing (SEE N90-27177 21-46)*, pp. 113–116.
- Constable, S. & Constable, C., 2004. Observing geomagnetic induction in magnetic satellite measurements and associated implications for mantle conductivity, *Geochem. Geophys. Geosyst.*, **5**, Q01006, doi:10.1029/2003GC000634.
- Egbert, G.D. & Booker, J.R., 1992. Very long period magnetotellurics at Tucson observatory—implications for mantle conductivity, *J. geophys. Res.*, **97**(B11), 15 099–15 112.
- Everett, M.E. & Schultz, A., 1996. Geomagnetic induction in a heterogeneous sphere: azimuthally symmetric test computations and the response of an undulating 660-km discontinuity, *J. geophys. Res.-Solid Earth*, **101**(B2), 2765–2783.
- Everett, M.E., Constable, S. & Constable, C.G., 2003. Effects of near-surface conductance on global satellite induction responses, *Geophys. J. Int.*, **153**(1), 277–286, doi:10.1046/j.1365-246X.2003.01906.x.
- Fujii, I. & Schultz, A., 2002. The 3D electromagnetic response of the Earth to ring current and auroral oval excitation, *Geophys. J. Int.*, **151**(3), 689–709.
- Grammatica, N. & Tarits, P., 2002. Contribution at satellite altitude of electromagnetically induced anomalies arising from a three-dimensional heterogeneously conducting Earth, using Sq as an inducing source field, *Geophys. J. Int.*, **151**, 913–923, doi:10.1046/j.1365-246X.2002.01817.x.
- Haber, E., Ascher, U.M. & Oldenburg, D., 2000. On optimization techniques for solving nonlinear inverse problems, *Inverse Problems*, **16**, 1263–1280.
- Haber, E., Ascher, U.M. & Oldenburg, D.W., 2004. Inversion of 3D electromagnetic data in frequency and time domain using an inexact all-at-once approach, *Geophysics*, **69**(5), 1216–1228.
- Hamano, Y., 2002. A new time-domain approach for the electromagnetic induction problem in a three-dimensional heterogeneous Earth, *Geophys. J. Int.*, **150**(3), 753–769.
- Hillery, M., O'Connell, R.F., Scully, M.O. & Wigner, E.P., 1984. Distribution functions in physics: fundamentals, *Phys. Rep.*, **106**, 121–167, doi:10.1016/0370-1573(84)90160-1.
- Hirsch, L. & Shankland, T., 1993. Quantitative olivine-defect role of Fe content, *Geophys. J. Int.*, **114**, 21–35.
- Hirsch, L., Shankland, A. & Duba, T.J., 1993. Electrical-conduction and polaron mobility in Fe-bearing olivine, *Geophys. J. Int.*, **114**, 36–44.
- Ichiki, M., Uyeshima, M., Utada, H., Guoze, Z., Ji, T. & Mingzhi, M., 2001. Upper mantle conductivity structure of the back-arc region beneath northeastern China, *Geophys. Res. Lett.*, **28**, 3773–3776, doi:10.1029/2001GL012983.
- Ishii, M. & Tromp, J., 2001. Even-degree lateral variations in the Earth's mantle constrained by free oscillations and the free-air gravity anomaly, *Geophys. J. Int.*, **145**, 77–96, doi:10.1046/j.1365-246X.2001.00385.x.
- Jordan, T.H., 1975. Lateral heterogeneity and mantle dynamics, *Nature*, **257**(5529), 745–750.
- Koyama, T., Shimizu, H. & Utada, H., 2003. Three-dimensional electrical conductivity structure beneath North Pacific by using a submarine cable network, Scientific Use of Submarine Cables and Related Technologies, 2003, in *The 3rd International Workshop*, Japan Marine Science and Technology Center, Yokosuka, Japan.
- Kuvshinov, A. & Olsen, N., 2006. A global model of mantle conductivity derived from 5 years of CHAMP, Ørsted & SAC-C magnetic data, *Geophys. Res. Lett.*, in press.
- Kuvshinov, A.V. & Pankratov, O.V., 1994. Electromagnetic induction in a spherical Earth with inhomogeneous conducting mantle: thin sheet forward problem, in *Proc. 12th Workshop on the Earth, Brest, France*, p. 83.
- Kuvshinov, A.V., Pankratov, O.V. & Singer, B.S., 1990. The effect of the oceans and sedimentary cover on global magnetovariational field distribution, *Pure appl. Geophys.*, **134**(4), 533–540.
- Kuvshinov, A., Utada, H., Avdeev, D. & Koyama, T., 2005. 3-D modelling and analysis of D_{st} C-responses in the North Pacific Ocean region, revisited, *Geophys. J. Int.*, **160**, 505–526, doi:10.1111/j.1365-246X.2005.02477.x.
- Kuvshinov, A., Sabaka, T. & Olsen, N., 2006. 3-D electromagnetic induction studies using the swarm constellation: mapping conductivity anomalies in the earth's mantle, *Earth Planets Space*, **58**, 417–427.
- Lay, T., 1994. The fate of descending slabs, *Annu. Rev. Earth planet. Sci.*, **22**, 33–61, doi:10.1146/annurev.ea.22.050194.000341.
- Lizarralde, D., Chave, A., Hirth, G. & Schultz, A., 1995. Northeastern Pacific mantle conductivity profile from long-period magnetotelluric sounding using Hawaii-to-California submarine cable data, *J. geophys. Res.-Solid Earth*, **100**(B9), 17 837–17 854.
- Mackie, R.L. & Madden, T.R., 1993a. 3-Dimensional magnetotelluric inversion using conjugate gradients, *Geophys. J. Int.*, **115**(1), 215–229.
- Mackie, R.L. & Madden, T.R., 1993b. Conjugate direction relaxation solutions for 3-D magnetotelluric modeling, *Geophysics*, **58**(7), 1052–1057.
- Mackie, R.L., Smith, J.T. & Madden, T.R., 1994. 3-Dimensional electromagnetic modeling using finite-difference equations—the magnetotelluric example, *Radio Sci.*, **29**(4), 923–935.
- Martinez, Z., 1998. Geomagnetic induction in multiple eccentrically nested spheres, *Geophys. J. Int.*, **132**, 96–110.
- Martinez, Z., 1999. Spectral-finite element approach to three-dimensional electromagnetic induction in a spherical Earth, *Geophys. J. Int.*, **136**, 229–250.
- Neal, S.L., Mackie, R.L., Larsen, J.C. & Schultz, A., 2000. Variations in the electrical conductivity of the upper mantle beneath North America and the Pacific ocean, *J. geophys. Res.-Solid Earth*, **105**(B4), 8229–8242.
- Newman, G.A. & Boggs, P.T., 2004. Solution accelerators for large-scale three-dimensional electromagnetic inverse problems, *Inverse Problems*, **20**, 151–170, doi:10.1088/0266-5611/20/6/S10.
- Olsen, N., 1999. Induction studies with satellite data, *Surv. Geophys.*, **20**(3–4), 309–340.
- Olsen, N., Luhr, H., Sabaka, T.J., Mandea, M., Rother, M., Toffner-Clausen, L. & Choi, S., 2006. CHAOS—a model of the Earth's magnetic field derived from CHAMP, Ørsted & SAC-C magnetic satellite data, *Geophys. J. Int.*, **166**(1), 67–75, doi:10.1111/j.1365-246X.2006.02959.x.
- Parker, R.L., 1994. *Geophysical Inverse Theory*, Princeton University Press, Princeton, New Jersey.

- Press, W.H., Teukolsky, S.A., Vetterling, W.T. & Flannery, B.P., 1992. *Numerical Recipes in Fortran 77—The Art of Scientific Computing*, 2nd edn, Cambridge University Press, Cambridge, UK.
- Rodi, W. & Mackie, R.L., 2001. Nonlinear conjugate gradients algorithm for 2-D magnetotelluric inversion, *Geophysics*, **66**(1), 174–187.
- Romanowicz, B., 2003. Global mantle tomography: progress status in the past 10 years, *Ann. Rev. Earth Planet. Sci.*, **31**, 303–328, doi:10.1146/annurev.earth.31.091602.113555.
- Sakamaki, T., Suzuki, A. & Ohtani, E., 2006. Stability of hydrous melt at the base of the Earth's upper mantle, *Nature*, **439**, 192–194, doi:10.1038/nature04352.
- Schmidt, A., 1895. Abhandl. Bayer Akad. Wiss. München II. Klasse 19, **1**.
- Schmucker, U., 1970. *Anomalies of Geomagnetic Variations in the South-western United States*, Vol. 13, 165pp., Bull. Scripps. Inst. Oceanogr., University of California Press, CA, USA.
- Schultz, A. & Larsen, J.C., 1987. On the electrical-conductivity of the mid-mantle: 1. Calculation of equivalent scalar magnetotelluric response functions, *Geophys. J. Int.*, **88**(3), 733–761.
- Schultz, A. & Larsen, J., 1990. On the electrical-conductivity of the mid-mantle: 2. Delineation of heterogeneity by application of extremal inverse solutions, *Geophys. J. Int.*, **101**(3), 565–580.
- Schultz, A. & Pritchard, G., 1999. A three-dimensional inversion for large-scale structure in a spherical domain, in *Three Dimensional Electromagnetics*, Vol. 7, pp. 451–476, eds Spies, B. & Oristaglio, M., Geophysical Developments Series, Society of Exploration Geophysicists.
- Schultz, A., Kurtz, R.D., Chave, A.D. & Jones, A.G., 1993. Conductivity discontinuities in the upper-mantle beneath a stable Craton, *Geophys. Res. Lett.*, **20**(24), 2941–2944.
- Shewchuk, J.R., 1994. An introduction to the conjugate gradient method without the agonizing pain, Technical Report, School of Computer Science, Carnegie Mellon University.
- Smith, J.T., 1996. Conservative modeling of 3-D electromagnetic fields: 2. Biconjugate gradient solution and an accelerator, *Geophysics*, **61**(5), 1319–1324.
- Su, W.-J. & Dziewonski, A.M., 1992. On the scale of mantle heterogeneity, *Phys. Earth planet. Inter.*, **74**, 29–54, doi:10.1016/0031-9201(92)90066-5.
- Tarits, P., 1994. Electromagnetic studies of global geodynamic processes, *Surv. Geophys.*, **15**(2), 209–238.
- Tikhonov, A.N., 1963. Solution of incorrectly formulated problems and the regularisation method, *Sov. Math. Dokl.*, **4**, 1035–1038.
- Toffelmier, D.A. & Tyburczy, J.A., 2007. Electromagnetic detection of a 410 km deep melt layer in the southwestern U.S., *Nature*, **447**, 991–994.
- Toh, H., Schultz, A., Uyeshima, M. & Fujii, I., 2002. Three-dimensional modelling of the Earth's mantle, in *Proceedings of the Ocean Hemisphere Project 2, Tokyo*.
- Utada, H., Koyama, T., Shimizu, H. & Chave, A.D., 2003. A semi-global reference model for electrical conductivity in the mid-mantle beneath the North Pacific region, *Geophys. Res. Lett.*, **30**(4), 1194–1197.
- Uyeshima, M. & Schultz, A., 2000. Geomagnetic induction in a heterogeneous sphere: a new three-dimensional forward solver using a conservative staggered-grid finite difference method, *Geophys. J. Int.*, **140**(3), 636–650.
- Velinsky, J. & Martinec, Z., 2005. Time-domain, spherical harmonic-finite element approach to transient three-dimensional geomagnetic induction in a spherical heterogeneous Earth, *Geophys. J. Int.*, **161**(1), 81–101.
- Velinsky, J., Everett, M.E. & Martinec, Z., 2003. The transient D_{st} electromagnetic induction signal at satellite altitudes for a realistic 3-D electrical conductivity in the crust and mantle, *Geophys. Res. Lett.*, **30**(7), 1355–1358.
- Velinsky, J., Martinec, Z. & Everett, M.E., 2006. Electrical conductivity in the Earth's mantle inferred from CHAMP satellite measurements; I. data processing and 1-D inversion, *Geophys. J. Int.*, **166**(2), 529–542, doi:10.1111/j.1365-246X.2006.03013.x.
- Weiss, C.J. & Everett, M.E., 1998. Geomagnetic induction in a heterogeneous sphere: fully three-dimensional test computations and the response of a realistic distribution of oceans and continents, *Geophys. J. Int.*, **135**(2), 650–662.
- Woodward, R.L., Forte, A.M., Su, W.-J. & Dziewonski, A.M., 1993. Constraints on the large-scale structure of the earth's mantle, *Evol. Earth Planets*, **14**, 89–109.
- Xu, Y.S., Poe, B.T., Shankland, T.J. & Rubie, D.C., 1998. Electrical conductivity of olivine, wadsleyite & ringwoodite under upper-mantle conditions, *Science*, **280**(5368), 1415–1418.
- Yoshimura, R. & Oshiman, N., 2002. Edge-based finite element approach to the simulation of geoelectromagnetic induction in a 3-D sphere, *Geophys. Res. Lett.*, **29**, 9–1.
- Zhang, T.S., 1991. Three-dimensional electromagnetic induction in a spherical Earth, *PhD thesis*, Geophysics Program, University of Washington.

APPENDIX A: EXPRESSIONS FOR THE FORWARD SOLVER AND THE JACOBIAN IN TERMS OF ELEMENTARY OPERATORS

It is possible to decompose the discretized Helmholtz operator into a combination of elementary sparse matrices, acting consecutively on the field vector. This may be done by constructing step by step each of the operators required to solve numerically the system of integral equations

$$\oint \mathbf{H} \cdot d\mathbf{l} = \iint \mathbf{J} \cdot d\mathbf{S},$$

$$\oint \mathbf{E} \cdot d\mathbf{l} = - \iint i\omega\mu\mathbf{H} \cdot d\mathbf{S},$$

$$\mathbf{J} = \sigma\mathbf{E}. \quad (\text{A1})$$

equivalent to the vector Helmholtz equation (4, see also U&S). Here, $\sigma = 1/\rho$.

We introduce discrete operators that represent mapping between the spaces \mathbb{G} , \mathbb{E} and \mathbb{F} , as defined in Section 3.2. In general, the letter \mathbf{D} for a matrix shall denote a square diagonal operator, with a subscript to indicate the nature of the values on the diagonal (see Table A1).

A1 Evaluating line integral $\oint \mathbf{H} \cdot d\mathbf{l}$

Let $\mathbf{C} : \mathbb{E} \rightarrow \mathbb{F}_1$ denote the sparse matrix (with non-zero elements ± 1) which computes the signed sum of components on H -edges of each prism, assigning the result to the corresponding H -faces. Both interior and boundary H -edges map to the interior faces. Note, that \mathbf{C} may be viewed as the discrete implementation of the curl operator, except that no length scales are involved—so that \mathbf{C} is, effectively, non-dimensional. The product $\mathbf{C}\mathbf{D}_E\mathbf{h}$ then implements the integral operator $\oint \mathbf{H} \cdot d\mathbf{l}$ locally around a face (Fig. A1), and current density on the E -edge normal to this face is $\mathbf{j} = \mathbf{D}_{SF}^{-1}\mathbf{C}\mathbf{D}_E\mathbf{h}$.

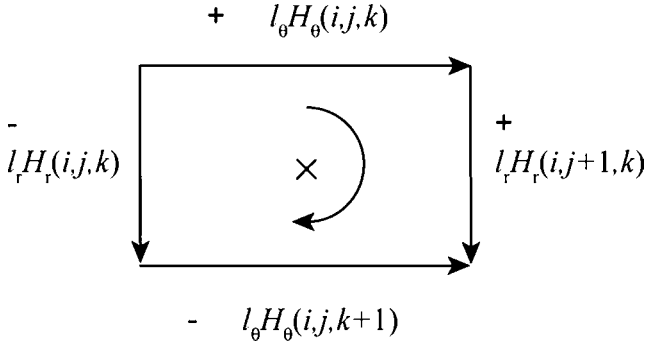
Electrical resistivity is defined on H -cell centres, but on the staggered-grid currents are naturally defined on H -faces (E -edges). Define $\mathbf{L} : \mathbb{G} \rightarrow \mathbb{F}_1$ to denote the operator that averages quantities in adjacent cells to their common face, weighting by the perpendicular cell length elements. This operator implements the resistivity averaging used in U&S,

$$\rho_{\text{face}} = \frac{l^+}{l^+ + l^-}\rho^+ + \frac{l^-}{l^+ + l^-}\rho^-, \quad (\text{A2})$$

where ρ^+ and ρ^- correspond to the resistivities of adjacent cells, and l^+ and l^- are, respectively, the perpendicular length elements in these cells. We also introduce a diagonal operator $\mathbf{D}_{L\rho} : \mathbb{F}_1 \rightarrow \mathbb{F}_1$, with the values of $\rho_{\text{face}} = \mathbf{L}\rho$ aligned along the diagonal. Then, the discrete estimate of the electric field $\mathbf{E} = \rho_{\text{face}}\mathbf{J}$ is $\mathbf{e} = \mathbf{D}_{L\rho}\mathbf{D}_{SF}^{-1}\mathbf{C}\mathbf{D}_E\mathbf{h}$.

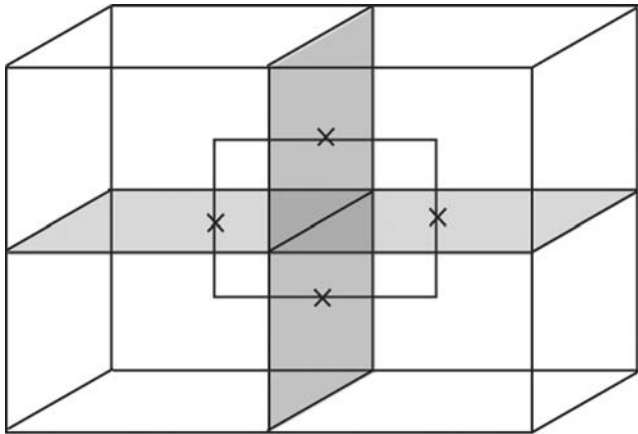
Table A1. Diagonal operators defined on the staggered-grid.

\mathbf{D}_{lE}	$: \mathbb{E} \rightarrow \mathbb{E}$	Pre-multiplies by edge length elements on H -edges
\mathbf{D}_{lF}	$: \mathbb{F}_i \rightarrow \mathbb{F}_i$	Pre-multiplies by edge length elements on E -edges
\mathbf{D}_{SF}	$: \mathbb{F}_i \rightarrow \mathbb{F}_i$	Pre-multiplies by surface area elements on H -faces
\mathbf{D}_{SE}	$: \mathbb{E} \rightarrow \mathbb{E}$	Pre-multiplies by perpendicular surface area elements on H -edges
$\mathbf{D}_{L\rho}$	$: \mathbb{F}_i \rightarrow \mathbb{F}_i$	Pre-multiplies by ρ on H -faces
$\mathbf{D}_{\rho F}$	$: \mathbb{F}_i \rightarrow \mathbb{F}_i$	Pre-multiplies by the weighted averages of ρ on H -faces
\mathbf{D}_l	$: \mathbb{E}_i \rightarrow \mathbb{E}_i$	Pre-multiplies by length elements. Acts on the interior components only. Shorthand notation for \mathbf{D}_{lE}
\mathbf{D}_S	$: \mathbb{E}_i \rightarrow \mathbb{E}_i$	Pre-multiplies by perpendicular surface area elements. Shorthand notation for \mathbf{D}_{SE}
\mathbf{D}_j	$: \mathbb{F}_i \rightarrow \mathbb{F}_i$	Pre-multiplies by the current density components $\mathbf{j} = \mathbf{D}_{SF}^{-1} \mathbf{C} \mathbf{D}_{lE} \mathbf{h}$

**Figure A1.** Operator \mathbf{C} can be used to evaluate the discrete approximation of $\oint \mathbf{H} \cdot d\mathbf{l}$; value assigned to face is a signed sum as indicated, and points into the diagram in accordance with the sense of integration around the contour.

A2 Evaluating line integral $\oint \mathbf{E} \cdot d\mathbf{l}$

Operator $\mathbf{C}^T : \mathbb{F}_i \rightarrow \mathbb{E}$ (the transpose of operator \mathbf{C}) locally implements a signed sum over four H -faces, that contain an H -edge, in the sense of integration around contour (Fig. A2). The discretization of the line integral $\oint \mathbf{E} \cdot d\mathbf{l}$, which maps the electric fields back from H -faces (E -edges) to H -edges, involves multiplication by $\mathbf{C}^T \mathbf{D}_{lF}$. Using the notation of eq. (A2), the length elements for E -edges may be computed as $(l^+ + l^-)/2$.

**Figure A2.** Operator \mathbf{C}^T maps the values on the four adjacent faces onto the centre edge of the 'paddle wheel', in accordance with the sense of integration around contour. This operator can be used to evaluate the discrete approximation of $\oint \mathbf{E} \cdot d\mathbf{l}$.

However, $\oint \mathbf{E} \cdot d\mathbf{l}$ is strictly only meaningful in the interior of the computational domain, that is, on interior H -edges (\mathbb{E}_i). Partitioning

$$\mathbf{C} \equiv (\mathbf{C}_i | \mathbf{C}_b), \quad (\text{A3})$$

where $\mathbf{C}_i : \mathbb{E}_i \rightarrow \mathbb{F}_i$ and $\mathbf{C}_b : \mathbb{E}_b \rightarrow \mathbb{F}_i$, the discretization can be written $\mathbf{C}_i^T \mathbf{D}_{lF} \mathbf{e}$.

A3 Decomposition of Helmholtz operator

Defining $\mathbf{D}_{\rho F} : \mathbb{F} \rightarrow \mathbb{F}$, such that

$$\mathbf{D}_{\rho F} = \mathbf{D}_{lF} \mathbf{D}_{L\rho} \mathbf{D}_{SF}^{-1}, \quad (\text{A4})$$

and collecting all the pieces defined above, the discretized vector Helmholtz eq. (4) can be written

$$\mathbf{C}_i^T \mathbf{D}_{\rho F} \mathbf{C} \mathbf{D}_{lE} \begin{bmatrix} \mathbf{h}_i \\ \mathbf{h}_b \end{bmatrix} + i\omega\mu_0 \mathbf{D}_{SE} \mathbf{h}_i = 0. \quad (\text{A5})$$

Noting eq. (A3), and moving the boundary components to the RHS, we obtain

$$(\mathbf{C}_i^T \mathbf{D}_{\rho F} \mathbf{C}_i \mathbf{D}_{lE} + i\omega\mu_0 \mathbf{D}_{SE}) \mathbf{h}_i = -\mathbf{C}_i^T \mathbf{D}_{\rho F} \mathbf{C}_b \mathbf{D}_{lE} \mathbf{h}_b, \quad (\text{A6})$$

where $\mathbf{h}_b = \mathbf{b}$ is determined by the boundary conditions. By comparison with eq. (21), $\mathbf{D}_l \equiv \mathbf{D}_{lE}$, we have

$$\mathbf{A}_{\rho,\omega} = \mathbf{C}_i^T \mathbf{D}_{\rho F} \mathbf{C}_i + i\omega\mu_0 \mathbf{D}_{SE} \mathbf{D}_{lE}^{-1}, \quad (\text{A7})$$

$$\mathbf{B}_\rho = \mathbf{C}_i^T \mathbf{D}_{\rho F} \mathbf{C}_b \mathbf{D}_{lE}. \quad (\text{A8})$$

A4 Using elementary operators to describe data sensitivities

The identities (23), (24) and (37) follow easily from the above decompositions. To derive the expression for \mathbf{E}_h (eq. 22), we note that

$$\mathbf{A}_{\delta\rho,0} \mathbf{D}_l \mathbf{h}_i + \mathbf{B}_{\delta\rho} \mathbf{b} = \mathbf{C}_i^T \mathbf{D}_{\delta\rho F} \mathbf{C} \mathbf{D}_{lE} \mathbf{h}. \quad (\text{A9})$$

Note that $\mathbf{j} = \mathbf{D}_{SF}^{-1} \mathbf{C} \mathbf{D}_{lE} \mathbf{h} \in \mathbb{F}_i$ is just a vector. For $\tilde{\mathbf{L}} : \mathbb{G} \rightarrow \mathbb{F}_i$ such that $\tilde{\mathbf{L}} \delta\rho = \mathbf{D}_{lF} \tilde{\mathbf{L}} \delta\rho$, recall the definition (A4) of $\mathbf{D}_{\delta\rho F}$ to write

$$\mathbf{D}_{\delta\rho F} \mathbf{C} \mathbf{D}_{lE} \mathbf{h} = \mathbf{D}_{lF} \mathbf{D}_{L\delta\rho} \mathbf{j} = \mathbf{D}_j \tilde{\mathbf{L}} \delta\rho, \quad (\text{A10})$$

where $\mathbf{D}_j = \text{diag}(\mathbf{j})$, and the expression (A9) holds with the operator $\mathbf{E}_h : \mathbb{G} \rightarrow \mathbb{E}_i$ being

$$\mathbf{E}_h = \mathbf{C}_i^T \mathbf{D}_j \tilde{\mathbf{L}}. \quad (\text{A11})$$

A5 Divergence correction

As evident from eq. (19), sensitivity calculations require solving a generalized forward problem, equivalent to eq. (4) with a non-zero interior forcing,

$$\nabla \times \rho(\nabla \times \mathbf{H}) + i\omega\mu_0\mathbf{H} = \mathbf{f}. \quad (\text{A12})$$

Taking the divergence of both sides of eq. (A12) yields

$$i\omega\mu_0\nabla \cdot \mathbf{H} = \nabla \cdot \mathbf{f}. \quad (\text{A13})$$

Thus, $\nabla \cdot \mathbf{H}$ in general is no longer zero for the generalized problem. Instead, the new identity (A13) should hold.

Numerically, denote the solution of the forward problem by $\tilde{\mathbf{h}}_i$ and the total interior forcing on the RHS by \mathbf{f} (so that $\mathbf{A}_{\rho,\omega}\tilde{\mathbf{h}}_i = \mathbf{f}$). Then we may use eqs (21) and (A13) to derive the identity

$$\nabla \cdot (\mathbf{D}_l^{-1}\tilde{\mathbf{h}}_i) + i\frac{\nabla \cdot \mathbf{f}}{\omega\mu_0} = 0, \quad (\text{A14})$$

for the generalized problem. In the adjoint formulation of eq. (39), the identity (A14) still holds true with ω negative. Therefore, a variant of the divergence correction method described by U&S can still be applied to accelerate convergence in the generalized forward and adjoint problems.